Biogeosciences, 23, 1383–1401, 2026
https://doi.org/10.5194/bg-23-1383-2026

Biogeosciences Open Access EGU

Imprint of minute hydrocarbon seepage on solid phase and pore water geochemistry in organic-poor subseafloor sediment

Ellen Schnabel[1], Jessica A. Stammeier[2], Stefanie Poetz[3], Kai Mangelsdorf[3], Aurèle Vuillemin[1], Rolando di Primio[4], Jens Kallmeyer[1], and the PROSPECTOMICS Consortium✚

[1]GFZ Helmholtz Centre for Geosciences, Section Geomicrobiology, Telegrafenberg, 14473 Potsdam, Germany
[2]GFZ Helmholtz Centre for Geosciences, Section Inorganic and Isotope Geochemistry, Telegrafenberg, 14473 Potsdam, Germany
[3]GFZ Helmholtz Centre for Geosciences, Section Organic Geochemistry, Telegrafenberg, 14473 Potsdam, Germany
[4]AkerBP, 1366 Lysaker, Norway
✚A full list of authors appears at the end of the paper.

Correspondence: Ellen Schnabel (eschnabe@gfz.de)

Received: 1 October 2025 – Discussion started: 7 October 2025
Revised: 26 January 2026 – Accepted: 26 January 2026 – Published: 23 February 2026

Abstract. In marine environments, small hydrocarbon (HC) fluxes through organic-poor sediments are often fully degraded by microorganisms before reaching the seabed. Yet, these fluxes influence sediment geochemistry by stimulating microbial activity. We analyzed 50 gravity cores from the southwestern Barents Sea, covering zones affected by inconspicuous HC seepage and unaffected reference zones. Using various organic and inorganic geochemical analyses of the sediment along with pore water geochemistry, we assess the effects of low-intensity seepage and identify potential geochemical signatures.

While analysis of the organic geochemical analyses provided limited insights, inorganic geochemical analyses revealed formation of minerals such as carbonates and sulfides, linked to microbial reductive processes. Element concentrations suggested that HC degradation leaves distinct signatures, particularly in redox-sensitive minerals. Pore water profiles in HC-affected zones showed significant variation, indicating carbonate precipitation. In contrast, sediments not affected by HC seepage displayed more uniform pore water profiles. Estimated fluxes of sulfate, calcium, and alkalinity varied notably between cores, particularly in HC-affected zones, suggesting local and potentially transient differences in seepage intensity.

While microbial HC degradation likely occurs deeper than our sampling interval, high-resolution geochemical analysis of both sediment fractions and pore water revealed a clear imprint of HC seepage. This imprint, reflected in authigenic minerals and pore water gradients, allows identification of past and present seepage activity, with authigenic minerals providing evidence for past seepage, and pore water profiles informing about ongoing seepage.

Key points.

- Even inconspicuous hydrocarbon seepage in organic-poor sediments modifies redox zonation, highlighting previously unrecognized biogeochemical sensitivity in low-flux systems.
- Subtle seepage causes distinct spatial heterogeneity in pore water chemistry and mineral formation patterns.
- Authigenic minerals and pore water gradients serve as complementary indicators of past and ongoing seepage.

1 Introduction

Marine subseafloor biogeochemical cycles are primarily governed by microorganisms (Joye et al., 2022), their metabolic activity is strongly controlled by availability and reactivity of sedimentary organic substrates. Due to lesser primary productivity of surface waters as compared to coastal areas (Chavez et al., 2011), in offshore sediments bioavailable organic matter (OM) is typically limited and becomes more recalcitrant with burial depth (Middelburg, 2018) due to lower

sedimentation rates (Røy et al., 2012). However, as all hydrocarbon reservoirs leak to some degree (Hunt, 1995; Heggland, 1998; Yergin, 2009), underlying hydrocarbon reservoirs will lead to buoyant hydrocarbon-rich fluids migrating upwards through the sediment column (Ciotoli et al., 2020). These HCs, even in trace amounts, represent an additional electron donor that can significantly fuel microbial activity (Zhang et al., 2022). Such influx of labile OM (i.e. seepage) leads to changes in microbial communities in terms of diversity and activity, which affect in turn specific physicochemical properties of the sediment, such as porosity, density, pore water geochemistry and mineral composition, (Abrams, 2005; Hvoslef et al., 1996; Joye, 2020). HC seepage through marine sediments fuels a variety of microbial processes, including sulfate reduction, fermentation, and methanogenesis (Joye, 2020; Schnabel et al., 2025a). Although these microbial processes are central to in situ biogeochemical transformations of OM on the continental shelf (Bradley et al., 2020), they are less pronounced in pelagic sediments wherein sulfate reduction becomes limited due to energy limitation (Vuillemin et al., 2020).Thus, at sites with low seepage rates HCs may be fully mineralized before reaching the sediment surface. Nevertheless, subtle but continuous HC fluxes influence sediment geochemistry and microbiology, not only in the direct vicinity of the HC source but also extending to the sediment surface (Rasheed et al., 2013; Joye et al., 2004).

Dissimilatory sulfate reduction (DSR), which is the predominant terminal electron-accepting pathway in oxygen-depleted, sulfate-containing shallow marine sediments (Kasten and Jørgensen, 2000; Bowles et al., 2014; Jørgensen et al., 2019), can be expected to be influenced by HC seepage and potentially be key in defining HC-related reductive diagenesis (Joye et al., 2004). Organoclastic sulfate reduction (OSR) relies on low molecular weight substrates derived from fermented particulate or dissolved OM (Jørgensen, 1982), whereas methanotrophic sulfate reduction is performed in conjunction with methane-oxidizing archaea (ANME) during anaerobic oxidation of methane (AOM) (Orphan et al., 2001). Thus, the influence of HC seepage on sulfate-reducing bacteria (Widdel et al., 2010) highly depends on whether light (i.e. gaseous, soluble) or heavy (i.e. long chain alkanes, aromatic rings) HCs are supplied. The types of seeping HCs and their subsequent microbial alteration can be resolved using mass spectrometry of sediment organic extracts, e.g. a shift from polar to less polar unsaturated HCs is observed during maturation (Hu et al., 2023), whereas the loss of hydrogen atoms in alkanes (via dehydrogenation) or oxygen incorporation in aromatic rings (cleavage via hydroxylation) reveal subsequent microbial alteration (Sert et al., 2020). Further geochemical effects inherent to sulfate reduction (SR) include an increase in pore water alkalinity, primarily as dissolved inorganic carbon (DIC) in the form of bicarbonate (HCO_3^-), and production of hydrogen sulfide (H_2S). Together these metabolic solutes create favorable sedimentary conditions for the precipitation of carbonate and sulfide minerals (Berner, 1981; Hinrichs et al., 1999; Lin et al., 2016), namely calcite ($CaCO_3$), mackinawite (FeS) and pyrite (FeS_2). Carbonates can record redox conditions at the time of formation (Vuillemin et al., 2023a and b) while their trace element compositions can indicate progressive alteration or diagenesis (Smrzka et al., 2019), in particular redox-sensitive trace metals (Smrzka et al., 2020; Tribovillard et al., 2013). Similarly, iron sulfides scavenge specific trace elements from the pore water (Huerta-Diaz and Morse, 1992), including chalcophilic and redox-sensitive bioessential metals (e.g. Mn, Mo, Cu, Zn).

Local redox conditions mediated by microbial processes also affect HC mobility as they promote the formation (e.g. carbonates) or dissolution (e.g. clays) of mineral barriers that adsorb HCs or impede their diffusion (Zhao et al., 2024; Eichhubl et al., 2009). For instance, the transition of smectite to illite decreases the mineral swelling capacity and reduces permeability (Kim et al., 2004; Dong et al., 2009). Such interplay of physical, geochemical and biological factors affects the migration of HCs and generates complex but characteristic flow patterns at active seep systems (de Groot et al., 2024). Thus, seep systems are characterized by pronounced spatial and temporal variations, permeability, fluid flow dynamics, and pressure conditions governing the rate at which HCs migrate upward (Foster et al., 2015; Leifer et al., 2004; de Groot et al., 2024), reasons for which characteristic HC seeps can be classified according to flux and surface manifestations (Table 1). Note that some seep-features like e.g. carbonate crusts or pockmarks remain even after active seepage stopped (Nickel et al., 2012, 2013).

According to our definition inconspicuous HC seeps are seeps where the seeping HCs lack visible surface manifestations. Instead, the HCs spread diffusely and are used up by biogeochemical processes so that the HCs do not reach the SWI. Although they likely imprint sediment geochemistry, they often remain undetected. Yet, any additional energy flux from weak seepage tends to promote complex interactions among local microbial communities adapted to substrate limitation or not, and influence the sediment geochemical dynamics, leading to fundamental metabolic and diagenetic processes (Abrams, 2020).

Here, we investigate how subtle, inconspicuous HC seepage influences the geochemical composition of both pore water and sediment. We analyzed 50 gravity cores collected from the southwestern Barents Sea, including 40 cores from zones affected by low-intensity seepage and 10 from unaffected reference zones. Given the challenges of deeper coring and the goal of minimizing environmental impact, we focused on the upper 3 m of sediment to determine whether direct or indirect effects of seepage could be detected. The large number of cores allows us to identify small-scale geochemical patterns and evaluate any spatial heterogeneity of discrete infiltrations. By combining organic and inorganic analyses of the sediment with pore water geochemistry, we decipher (I) the extent to which inconspicous HC seeps af-

Table 1. Classification of hydrocarbon seeps based on methane flux and associated surface manifestations. The table is compiled after (Judd and Hovland, 2009; Etiope, 2015). The flux range between inconspicuous- and moderate-flux seeps (1 to 100 mmol m^{-2} d^{-1}) represents a conceptual transition zone, where current data are insufficient to establish a clear distinction.

Seep type	Inconspicuous seeps	Moderate seeps	High flux seeps
Flux range	<1 mmol m^{-2} d^{-1}	0.1–1 mol m^{-2} d^{-1}	1–10 mol m^{-2} d^{-1}
Pockmarks	No pockmarks	Small, less deeply pronounced pockmarks	Larger, deeper and more numerous pockmarks, clearer
Methane and gas bubbles	No bubbles	Few, smaller bubbles, mostly sporadic	Frequent and larger bubbles, continuous gas flow
Chemical changes	No or minimal chemical changes on the surface	Low concentration of carbonates and sulfides	Significant enrichment of carbonates and sulfides, possible mineral deposits
Biogenic hotspots	No biological hotspots	Local colonization of methane-oxidizing bacteria	Intensive biological activity, larger hotspots with more diverse methane-fed fauna (e.g. mussels)
Gas hydrates	No gas hydrates	Little or no gas hydrates	Possible presence of gas hydrates, especially at low temperatures and high methane flow

fect the distribution of key geochemical species (e.g. sulfide, methane, calcium, alkalinity) in pore water and sediment, and (II) how these parameters vary spatially across and between seepage and reference zones.

2 Material and Methods

2.1 Geological setting and sampling

The Barents Sea is an epicontinental shelf sea bordered by the Norwegian Sea to the southwest, the Arctic Ocean to the north, and the Russian archipelago of Novaya Zemlya to the east. It rests on a Caledonian basement formed during Paleozoic orogenies, but its present structural configuration mainly reflects Mesozoic and Cenozoic tectonic phases, including episodes of uplift, subsidence, tilting, and erosion. This has resulted in a varied structural landscape with elevated highs (e.g., the Loppa High) and intervening sedimentary basins (Doré, 1995; Gabrielsen et al., 1990; Johansen et al., 1993; Larssen et al., 2002; Faleide et al., 1984). During the Mesozoic, organic-rich marine shales were deposited under greenhouse climate conditions with high marine productivity and fluctuating sea levels. These shales – particularly the Upper Jurassic Hekkingen Formation, act as the principal source rocks for hydrocarbons in the southwestern Barents Sea (Marín et al., 2020; Langrock et al., 2003). Burial over millions of years led to thermal maturation, hydrocarbon generation, and subsequent migration into structural traps, such as those found in the Johan Castberg and Snøhvit fields. In the Quaternary, the region was repeatedly covered by ice sheets. During the last glaciation, the Barents Sea was overridden by grounded ice, leading to significant glacial erosion. Consequently, the modern sediment cover on structural highs is often very thin and sediments primarily consist of glacial and glaciomarine silty clays, dropstones, and fine sands derived from the erosion of local and distal bedrock during glacial advance and retreat. These surficial sediments are typically organic-poor, reflecting both their glacial origin and limited biological productivity during deposition (Knies and Martinez, 2009; Nickel et al., 2013; Sættem et al., 1991; Elverhøi and Solheim, 1983).

During an expedition to the SW Barents Sea in October/November 2021, we collected a total of fifty gravity cores, ranging from 0.5 to 3 m in length, within three zones with known underlying HC reservoirs (Z01, Z10, Z12), as well as two zones (Ref5, Ref6) with no HC reservoirs, labelled hereafter as HC zones and reference zones (Fig. 1a). The coring sites lie at a water depth of approximately 350 m (Fig. 1b). Immediately after retrieval of a core (Fig. 1c), the lowermost 20 cm of the core were cut off, the sediment was pushed out of the liner and the outer 1–2 cm were scraped off with a sterile spatula to remove possible contamination. Using 5 mL cut-off syringes, 3 cm^3 of sediment were transferred into a 10 mL glass crimp vial containing saturated NaCl solution. The vials were immediately sealed with thick butyl rubber stoppers, crimped, and stored upside down without headspace until gas analyses in the home lab. An additional 2 cm^3 of sediment was transferred into a 15 mL centrifuge tube containing 8 mL of NaCl-formalin fixative solution (25 g L^{-1} NaCl, 20 g L^{-1} formalin) and thoroughly homogenized for cell counting. The remaining sediment was aliquoted for solid phase geochemistry. The rest of the core was cut into 1 m sections, capped and stored on deck, as air, water and sediment temperature were all around 5 °C.

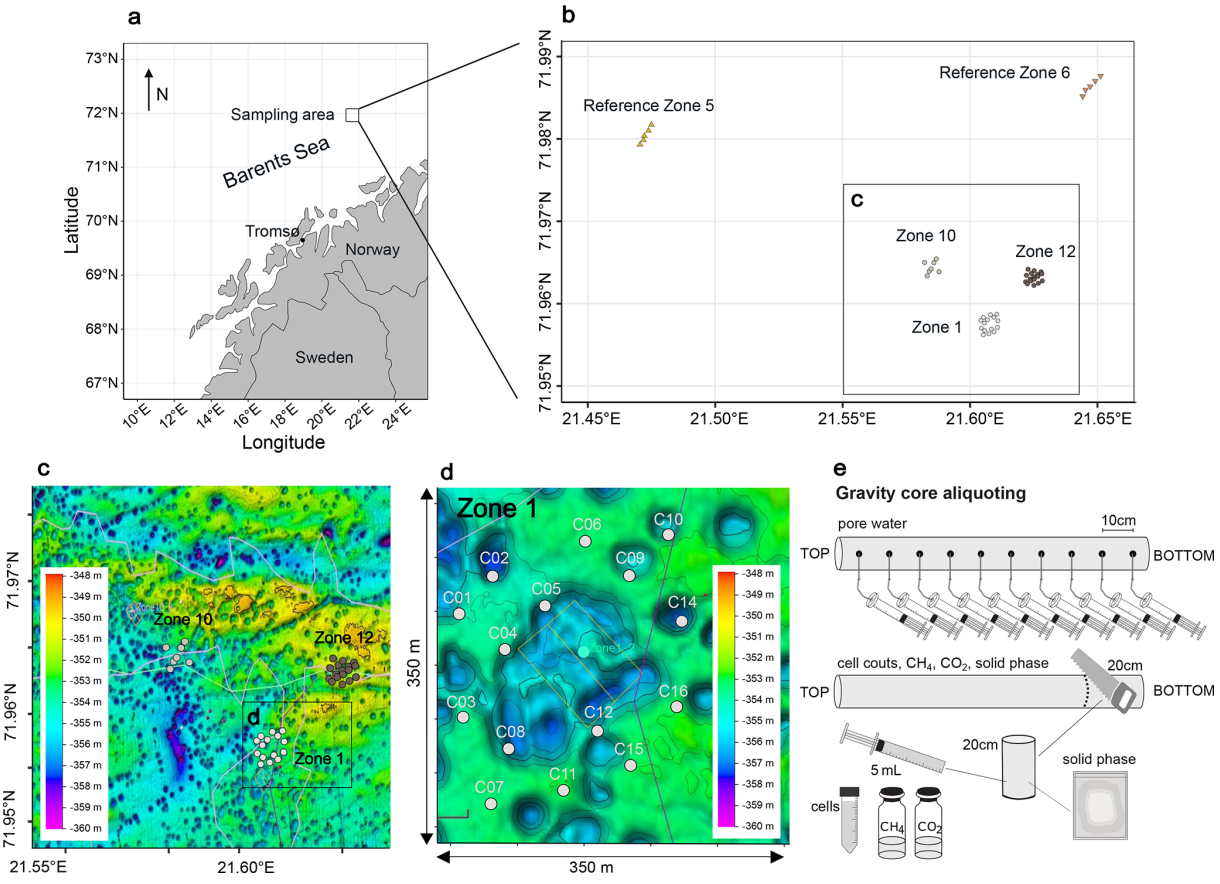

Figure 1. Sampling locations. **(a)** Map of the Norwegian coast. The square marks the sampling area. Fifty cores were retrieved from three HC-affected zones (Zone 1, Zone 10, Zone 12) and two reference zones (Ref 5, Ref 6). **(b)** Bathymetric map of the 3 HC-affected zones. Each zone was sampled in a grid of cores, Zone 1 is enlarged here as an example. The missing samples in the middle are due to the increased occurrence of dropstones in this area, preventing the deployment of a gravity corer. **(c)** Schematic overview of the sampling strategy. This figure was modified after (Schnabel et al., 2025a).

Pore water was extracted on board, with extractions initiated within two hours of core retrieval. Rhizon pore water samplers (Rhizosphere Research Products B.V., Netherlands; Seeberg-Elverfeldt et al., 2005) were inserted into the intact sediment core through small holes drilled in ca. 10 cm intervals. Pore water collection took between 12 and 24 h. The collected pore water samples were 0.22 µm-filtered (Merck Millex™-GS Sterile Syringe Filter Unit, MCE) and aliquoted for different downstream analyses. For anion, cation, and trace element measurements, 1.5 mL each was collected in plastic screw-cap vials without any further treatment. These samples were kept anoxic until analysis. For alkalinity measurements, 2 mL of pore water were filled into a glass vial pre-filled with 50 µL of saturated $HgCl_2$ solution to prevent bacterial activity (Edenborn et al., 1985) and closed without any headspace. For quantification of dissolved hydrogen sulfide, we transferred 1.5 mL of pore water into a 2 mL plastic screw-cap vial and added 200 µL $ZnCl_2$ (20 % weight vol^{-1}). All samples were stored at +4 °C until analysis in the home lab.

2.2 Methane and carbon dioxide concentrations

Prior to measurement, we introduced 3 mL of ultrapure helium gas as headspace while withdrawing the same amount of NaCl solution from the crimped vial. To equilibrate dissolved gases with the headspace, the content of the vials was mixed at 220 rpm on an orbital shaker for 18 h, and further vortexed to break up the remaining small clayey aggregates. A 250 µL sample of the headspace gas was then extracted and introduced into a 7890A Gas Chromatography System, which was equipped with both a flame ionization detector (FID) and a thermal conductivity detector (TCD), along with an HP PLOT Q column (all from Agilent). The oven temperature was set to 50 °C, the flow rate was maintained at 17.2 mL min^{-1}, and the pressure was held at 13 psi. Both detectors operated at 200 °C with flow rates of 40 mL min^{-1} (FID) and 15 mL min^{-1} (TCD). Calibration of the system was performed by injecting pure analytical standards with CO_2 concentrations of 310 and 5270 ppm, as well as CH_4 concentrations of 10 and 5170 ppm. The initial CH_4 and CO_2

concentrations were converted from ppm to molar concentrations using the ideal gas law.

2.3 Cell counting

Total cell counts were conducted following a protocol based on Kallmeyer et al. (2008). Sediment samples were initially diluted at a ratio of 1 : 100 using a 25 g L^{-1} NaCl solution. 25 µL of the resulting slurry were uniformly distributed onto black 0.2 µ m polycarbonate Cyclopore membrane filters (Whatman International Ltd, Maidstone, UK) via vacuum filtration. For cell visualization, filters were stained with a mixture consisting of SYBR Green I (10 µL; Molecular Probes, Eugene, USA), phenylenediamine (100 µL), glycerol (300 µL), Milli-Q water (300 µL), and 300 µL of VECTASHIELD® Antifade Mounting Medium (H-1000-10, Vector Laboratories, Burlingame, USA). A volume of 15 µL of this staining solution was applied to each filter. The counting was performed using an epifluorescence microscope (Leica DM2000, Wetzlar, Germany) by counting cells in 200 fields of view. Cell abundances were calculated as log10 cells per cm^3 of sediment, based on triplicate measurements, with standard deviations consistently remaining below 15 %.

2.4 Pore water geochemistry

Dissolved sulfate was quantified via suppressed Ion Chromatography (column: SykroGel A × 300 AB-A01; eluent: 7.3 mg L^{-1} NaSCN and 636 mg L^{-1} $NaCO_3$; pump rate 1 mL min^{-1}; injection volume 50 µL). The detection limit was 5 µM. Samples were measured in triplicate, with average relative standard deviations consistently below 3 %.

Cation and trace elemental concentrations in the pore water were determined using high-resolution inductively coupled plasma mass spectrometry (HR-ICP-MS, ELEMENT 2XR, Thermo Scientific, Waltham, USA) at the ElMiE-labs at GFZ after acidifying the samples with ultrapure HNO_3 immediately prior to analysis. Until analysis, the samples were kept anoxic to prevent precipitation and potential alteration of the metal concentrations. 100 µL of pore water was doped with 10 µL of an indium (In) standard solution at a concentration of 100 µg L^{-1} and the samples where diluted with 2 vol % ultrapure HNO_3. Trace elements were quantified by external calibration using single-element standards, carefully matched to the sample matrix. The acid blank was subtracted from each measurement. The detection limits for the applied ICP-MS routine typically ranged between 0.5 and 1 ng g^{-1}, for the analytes. Measurement uncertainty, referring to the repeatability of the measurements, was about 2 %–5 % for all analyses.

Iron concentrations were analyzed separately using spectrophotometry, following the protocol described by Viollier et al. (2000). The detection limit of this method is 0.25 µM and the measurement uncertainty was approximately 5 % for all analyses. Sulfide was determined photometrically according to Cline (1969). The detection limit is 0.1 µM. All samples were measured in triplicates and the results were averaged with a standard deviation $\leq$ 3.5 %. Alkalinity was determined via titration using the Visocolor HE alkalinity AL 7 kit (Macherey-Nagel GmbH) adapted to the sample volume of 500 µL. The detection limit is 0.15 mM and triplicate measurements differed by less than 3 %.

2.5 Sediment inorganic fraction

For XRF analysis, approximately 30 g of sediment material was freeze-dried, ground in agate mortars using a Fritsch Pulverisette 5 planetary mill at 300 rpm for 5 min, sieved through a 63 µm stainless steel mesh, and then melted with two Fluxana reference materials to form glass discs. These discs were analyzed using an AXIOS X-ray fluorescence (XRF) advanced spectrometer (Malvern Panalytical, United Kingdom), equipped with an End-window RH X-ray tube SST-mAX at a 4 kW output. Elemental proportions were determined for major elements as oxides in weight % [wt %] (i.e. SiO_2, Al_2O_3, Fe_2O_3, MnO, MgO, CaO, Na_2O, K_2O, P_2O_5, TiO_2, SO_3, loss on ignition (LOI)), and trace elements in parts per million [ppm] (i.e. Ba, Cr, Zn, Ga, Nb, Ni, Rb, Sr, V, Y, Zr). Quantification limits for major elements were 0.02 wt % and approximately 10 ppm for trace elements. LOI was determined based on the mass difference before and after fusion. Reproducibility was evaluated using reference materials and better than 2 % for all major elements.

2.6 Statistical and geostatistical analyses

Min-max normalization was applied to the XRF dataset, scaling all variables to a range between 0 and 1. PCA was then performed using the prcomp() function in R with centering and scaling enabled to identify patterns and relationships among chemical species in the solid sediment phase, reducing the data's dimensionality and highlighting key variability across samples. This analysis provided further insight into the underlying structure of the data, complementing the subsequent visualizations. For ternary visualization, selected standardized parameters were then proportionally scaled to sum to 100 %. In some cases, the resulting values of multiple compounds (e.g., those associated with specific mineral groups like carbonates) were summed. Thus, the ternary diagrams reflect only relative patterns and should not be interpreted in terms of absolute abundances.

We applied Mann–Whitney U tests (Mann and Whitney, 1947) using the function wilcox.test() to XRF and pore water data to assess whether the median values of individual chemical species differed significantly between groups. This non-parametric test was used to evaluate differences in concentration gradients in the pore water and absolute concentrations in the solid sediment phase between HC-affected zones (Z01, Z10, Z12) and reference sites (Ref5, Ref6), as well as among and within individual zones and sediment cores.

To assess differences in variability (i.e. variance), we also used the Brown-Forsythe test (Brown and Forsythe, 1974) applying the leveneTest() function. This test allowed us to assess whether the variance in chemical species concentrations – reflecting chemical heterogeneity – varied significantly between zones. Finally, Pearson correlation analyses (Pearson, 1895; Sedgwick, 2012) were conducted on the pore water data to explore linear relationships among chemical species. Two analytical levels were considered: (1) correlations within individual sediment cores, and (2) correlations across all cores from the same sampling zone (e.g. all cores from Z01). All statistical and geostatistical analyses were performed using R version 4.2.0 (R Core Team, 2022).

Diffusive fluxes of sulfate, alkalinity, and calcium across the sediment–water interface were calculated based on Fick's first law of diffusion using the linear concentration gradients. Molecular diffusion coefficients were taken from Schulz (2006) and subsequently adjusted for sediment conditions following Iversen and Jørgensen (1993). To visualize spatial patterns in fluxes of sulfate, alkalinity, and calcium, we applied ordinary kriging using the gstat package in R (Pebesma, 2004). First, empirical variograms were calculated from spatially referenced flux measurements. Several theoretical variogram models (spherical, exponential, Gaussian, and Matérn) were fitted and compared. The best-fitting model was selected based on convergence criteria and plausibility of the sill and range parameters. This model was then used to interpolate flux values across a regular spatial grid covering the study area. The resulting kriging maps (Matheron, 1963) provided continuous spatial representations of flux gradients and enabled the identification of heterogeneities between hydrocarbon seep zones and reference sites. Visualizations were created using the ggplot2 package (Wickham, 2016).

2.7 Sediment organic fraction

Molecular-level insights into the organic geochemistry of sediments were obtained for solvent-extractable OM using Fourier Transform Ion Cyclotron Resonance Mass Spectrometry (FT-ICR-MS). Based on geochemical pore water profiles, a subset of 11 representative samples consisting of three samples from each of the three HC zones (Z01, Z10, Z12) and one sample from each of the two reference zones (Ref5, Ref6) was selected from the total of 50 sediment cores. For each sample, approximately 10 g of sediment were freeze-dried, milled, and the organic content was extracted using a Soxhlet extractor following a procedure described by Poetz et al. (2014). The extraction was performed with a solvent mixture composed of dichloromethane and methanol ($v/v = 99:1$) at 40 °C for 24 h. The extracts were then analyzed at ultra-high mass resolution using a Bruker Daltonik Solarix 12T FT-ICR-MS. Ionization was carried out using an Apollo II ESI source and an APPI-II source (all from Bruker Daltonik GmbH, Bremen, Germany).

For electrospray ionization (ESI−), nitrogen was used as the nebulizing gas at a flow rate of 4 L min^{-1} at 220 °C and a pressure of 1.4 bar. The capillary voltage was set to 3000 V, and the collision-induced dissociation (CID) voltage was 60 V. The samples were infused at a flow rate of 2.5 µL min^{-1} using a Hamilton syringe pump. The spectra were recorded in broadband mode using 8-megaword data sets. The ion accumulation time was 0.05 s, and a total of 200 scans were collected into the mass spectrum, covering a mass-to-charge ratio (m/z) range of 150–1000. For atmospheric pressure photoionization (APPI+), nitrogen was used as the nebulizing gas at a flow rate of 3 L min^{-1} at 210 °C and a pressure of 12.3 bar. The capillary voltage was set to −1000 V, and the CID voltage was 30 V. The samples were infused at a flow rate of 20 µL min^{-1} using a Hamilton syringe pump. The spectra were recorded in broadband mode using 8-megaword data sets. The ion accumulation time was 0.05 s, and a total of 300 scans were collected into the mass spectrum, covering an m/z range of 147–1500.

The resulting spectra were internally recalibrated (quadratic) with a standard deviation error of <0.02 ppm, and only m/z values with a signal-to-noise ratio >9 were exported for formula assignment. Formula assignment was performed using a combination of Bruker Analysis and Microsoft Excel, considering the isotopes ^{12}C and ^{13}C and the elemental ranges $C_xH_yN_{0–2}O_{0–10}S_{0–2}Na_{0–1}$. The mass tolerance was set to 5 ppm.

3 Results

3.1 Methane and carbon dioxide concentrations and cell abundances

All samples contain measurable methane concentrations, ranging from 0.08 to 19.79 µM. While samples from reference sites contain less than 5 µM of methane, higher concentrations are restricted to few samples from HC-affected sites, all located deeper than 100 cm below seafloor (cmbsf). CO_2 was detectable in all samples, with concentrations ranging from 29 to 512 µM, without any site-specific trend (Supplement Fig. S1). This is likely due to carbonate buffering, with dissolved CO_2 equilibrating with bicarbonate and carbonate in pore water at both HC-affected and reference sites. In both cases, low gas concentrations prevented measurement of their stable isotopic signatures.

Total cell counts are approximately 10^7 cells cm^{-3} across all sediment cores, with no significant variation with depth (Supplement Fig. S2). The mean deviation of cell counts within samples is around 12 %.

3.2 Pore water profiles

Both sulfate and alkalinity concentrations exhibit strong linear decreasing and increasing trends ($R^2 \geq 0.85$) with depth (Fig. 2a and b), respectively. The gradients are steeper in the

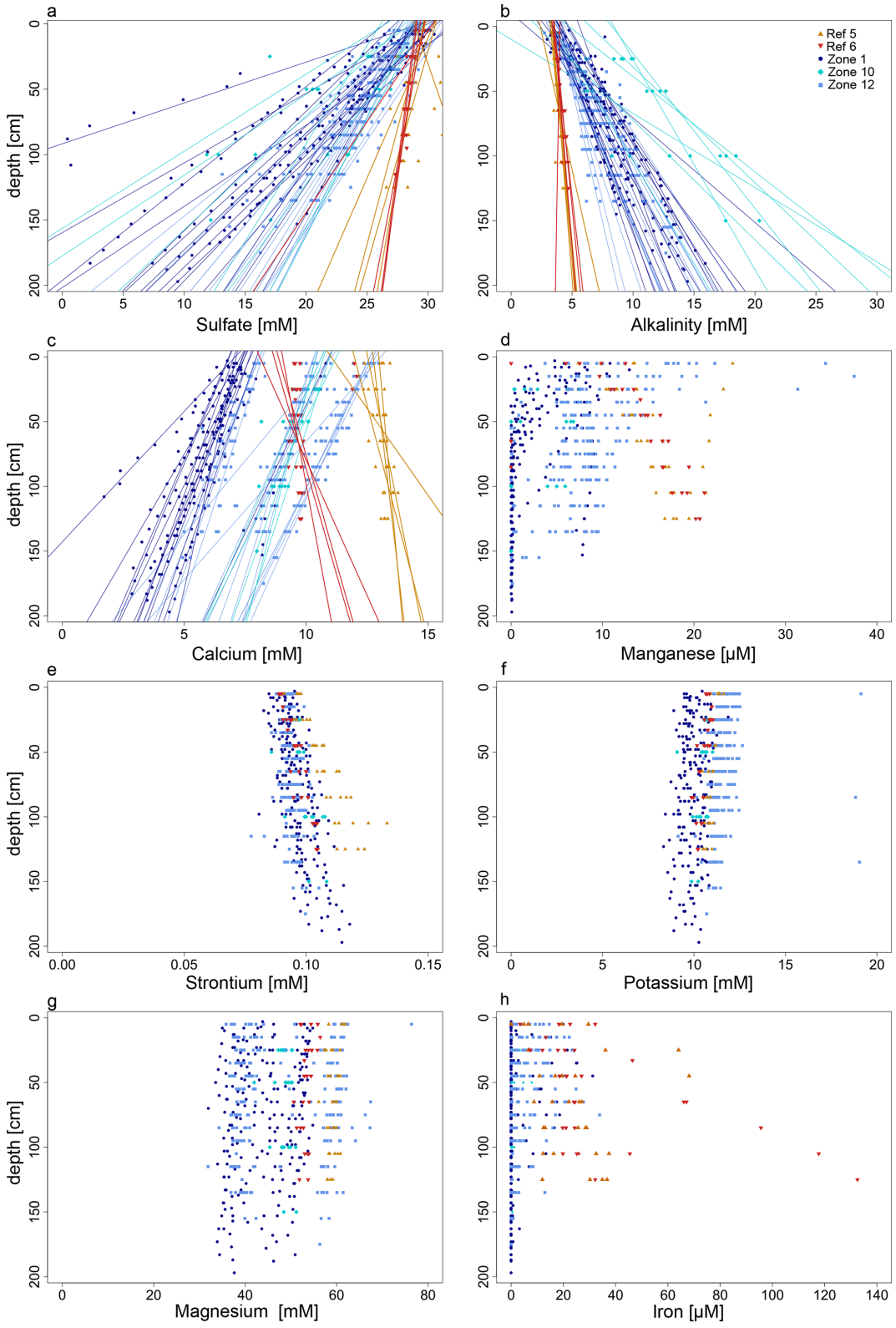

Figure 2. Pore-water profiles for some representative parameters. The profiles for sulfate concentrations **(a)**, alkalinity **(b)**, and calcium **(c)** show both data points and regression lines (R^2>0.8). The regression lines for HC-affected zones (Zone 1, Zone 10, Zone 12) show steeper gradients compared to those from reference zones (Ref 5, Ref 6). The profiles for magnesium **(d)**, strontium **(e)**, potassium **(f)**, magnesium **(g)**, and iron **(h)** are shown as data points due to the insufficient R^2 value of their respective regression lines.

HC-affected zones compared to reference zones. Based on linear extrapolation, sulfate depletion would be reached at ca. 3 and 12 mbsf in HC and reference zones, respectively. Sulfide concentrations are below the detection limit (1 µM) in all cores from reference zones and in most of the cores from Z12 (only 2 out of 17 cores have detectable sulfide; Supplement Fig. S3). In contrast, in most cores from Z01 (12 out of 15) and Z10 (4 out of 7), sulfide concentrations increase with depth.

In the reference zones concentrations of pore water Ca^{2+} increase with depth (Fig. 2c, Supplement Fig. S3), but decrease in the HC-affected zones. For Mn^{2+} concentrations also increase with depth in the reference zones (Fig. 2d, Supplement Fig. S4). In most of the cores from HC-affected zones, Mn^{2+} pore water profiles show a decreasing trend with depth, but with distinct patterns, of which each one is predominant in a different sampling zone: (1) in Z01 many profiles show concentrations decreasing from ca. 15 µM at the SWI to near zero at ca. 75 cmbsf; (2) in Z12 concentrations decrease from ca. 15 µM at the SWI but then stabilize around 5 µM at 1 mbsf; (3) in Z10 and Z12 some concentrations profiles remain constant around 7 mM throughout depth.

Pore water concentrations for Cu^{2+}, Si^{4+}, Zn^{2+}, Mg^{2+} and K^{+} remain almost unchanged with depth in both HC-affected and reference zones (Fig. 2e–g, Supplement Figs. S4–S5), whereas Sr^{2+} concentrations increase in cores from both HC-affected zones and reference zones, but more pronounced for the latter (Fig. 2e). Dissolved Fe^{2+} is rarely detectable in cores from the HC-affected zones and falls below detection limit within the upper 1 mbsf (Fig. 2h). In most cores from reference zones, pore water Fe^{2+} is detectable and concentrations increase with depth. Ba^{2+} was measurable only in few cores from Z01, with concentrations increasing with depth (Supplement Fig. S4). With few exceptions, Ni^{2+} and As^{2+} remain below the detection limit in all samples at all depths.

3.3 Statistical analyses of inter- and intrazonal variations

3.3.1 Comparative analysis of pore water geochemistry

The Mann-Whitney U tests (Mann and Whitney, 1947) confirmed statistical significance for steeper sulfate and alkalinity gradients (Fig. 2, Supplement Table S2) in HC-affected zones ($p_{SO_4} = 3.86 \times 10^{-10}$, $p_{alk} = 2.74 \times 10^{-5}$); opposite trends in Ca^{2+} profiles ($p_{Ca} = 1.40 \times 10^{-4}$); and different pore water gradients in Mn^{2+} concentrations ($p_{Mn} = 5.38 \times 10^{-6}$), assuming linear profiles which in some cases did not provide the best fit (Fig. 2, Supplement Fig. S4 and porewater profile descriptions in Sect. 3.1). The results for manganese should therefore be considered as approximations.

The Brown-Forsythe tests (Brown and Forsythe, 1974) further confirmed that the variance for pore water SO_4^{2-}, alkalinity, Ca^{2+}, and Mn^{2+} gradients is smaller within reference zones (all p-values < 0.05, Supplement Table S3) than within HC-affected zones (Fig. 2). In addition, a comparison of the variances across individual HC zones and reference zones indicates significant differences in most instances.

Kriging plots for sulfate, alkalinity and calcium fluxes (which are proportional to their gradients) enabled the visualization of spatial variations over the entire study area and within the sampling zones (Fig. 3). The resulting patterns of variability align with previous statistical tests and highlight the different spatial heterogeneity between reference and HC-affected areas, with notably a stronger variability among those exposed to seepage.

3.3.2 Pore water species within and across cores

We also performed intra- and intervariation analyses, i.e. we investigated the correlation of chemical species within each core using Pearson Correlation (Pearson, 1895; Sedgwick, 2012). We found a strong correlation (average $|r| > 0.86$) between sulfate, alkalinity and calcium and, to a lesser extent (average $|r| > 0.66$) with manganese in almost every individual core from HC zones. In contrast, within reference zones, we only found correlations between alkalinity and sulfate (average $r > -0.76$) as well as alkalinity and manganese (average $r > 0.86$) (Supplement Table S4).

To determine whether concomitant biogeochemical processes may occur in different cores, we assessed the correlation between pore water gradients for each of the 5 sampling zones separately, resulting in 10 combinations of alkalinity, sulfate, manganese, calcium, and sulfide. For cores from reference zones, a negative correlation between sulfate and alkalinity was observed ($r = -0.80$ and -0.85 for Ref5 and Ref6). In addition, for Ref5, additional correlations were found between sulfate and manganese ($r = -0.99$), alkalinity and calcium ($r = -0.86$) and alkalinity and manganese ($r = 0.78$). For cores from the three HC zones, no significant correlations ($r < 0.7$) were found between geochemical species, except at Z10 between sulfate and alkalinity ($r = -0.89$), alkalinity and sulfide ($r = 0.77$) (Supplement Table S4).

3.3.3 XRF elemental concentrations of the sediment inorganic fraction

CaO and SO_3 concentrations are significantly higher (Mann-Whitney U test, $p < 0.05$) in sediments from HC-affected than reference zones. Despite similar behavior as alkaline-earth elements, Ba ($p = 0.11$) and Sr ($p = 0.17$) were only slightly more abundant in sediments exposed to seepage. Conversely, the relative abundance of Fe_2O_3, P_2O_5, Ti, Cr, and Zn is higher ($p < 0.05$) in cores from reference zones, while Al ($p = 0.06$), Ni ($p = 0.05$), Mn ($p = 0.12$), and V ($p = 0.05$) show a tendency towards higher relative abun-

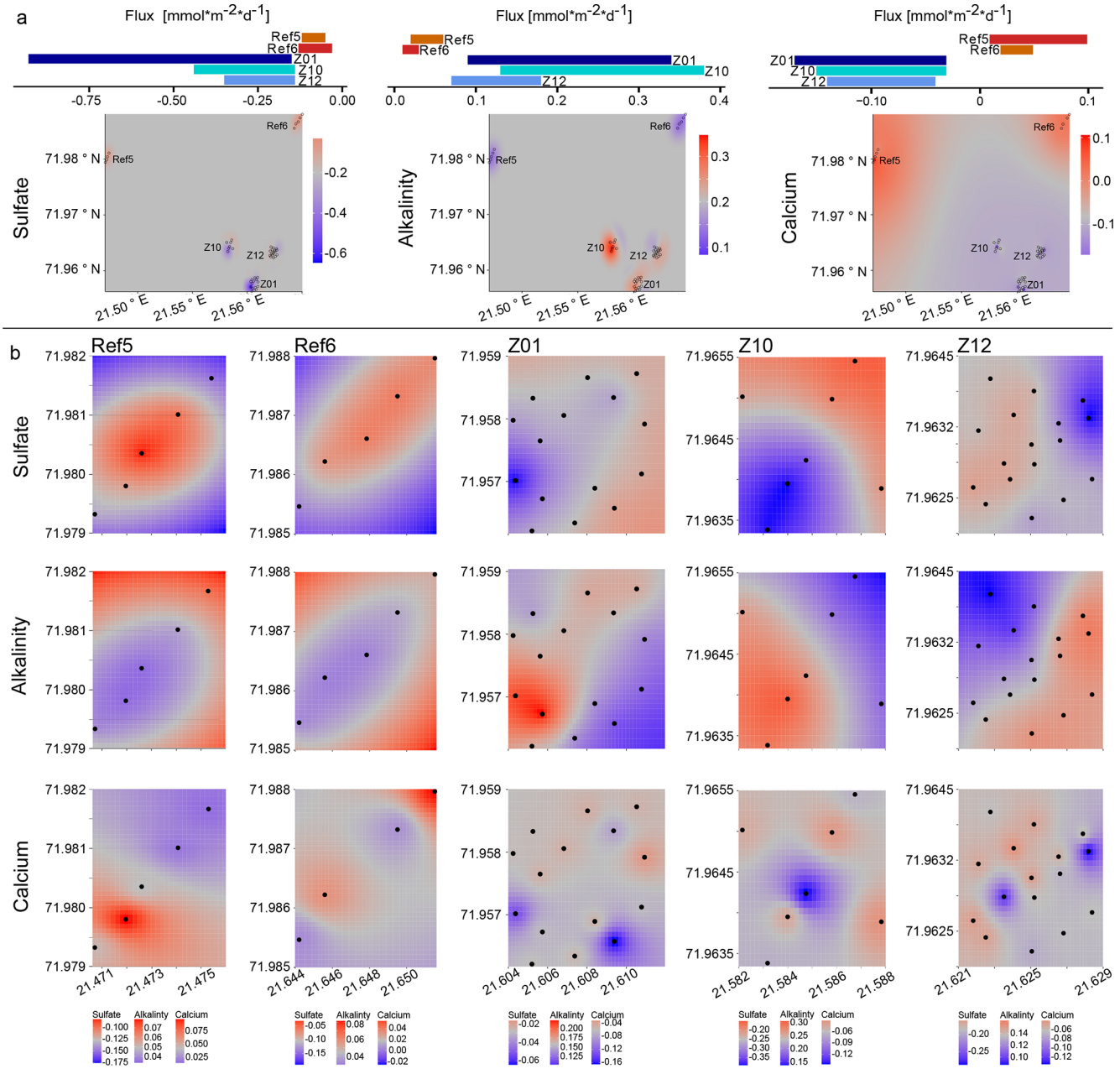

Figure 3. Spatial variability and flux patterns of sulfate, alkalinity, and calcium across different zones. **(a)** Bar plots show the mean areal fluxes (mmol m^{-2} d^{-1}) of sulfate (left), alkalinity (middle), and calcium (right) at the five zones (Ref5, Ref6, Z01, Z10, Z12). Kriging-interpolated maps illustrate the spatial distribution of these fluxes across the study area. Color gradients indicate the direction and magnitude of fluxes. **(b)** Detailed kriging maps of sulfate (top row), alkalinity (middle row), and calcium (bottom row) fluxes at each zone. Each column corresponds to one zone, showing localized spatial variability in solute fluxes. Black dots indicate the sampling sites.

dances. The loss on ignition (LOI) is significantly higher ($p<0.05$) in cores from reference zones.

Significant differences ($p<0.05$) revealed by the Brown-Forsythe variance homogeneity test included Ba and SO_3 concentrations at seepage and reference zones, highlighting higher variance among cores from HC-affected zones. Variance in CaO concentrations appeared non-significant ($p =$ 0.09). Major and trace element in ternary diagrams (Fig. 4) confirm this, as the variance (scatter) is noticeably greater in the HC zones compared to the reference zones. Despite considerable overlap, this observation is consistent with the results of the Brown-Forsythe test, illustrating the lower variance across samples from reference zones compared to HC zones. This pattern is further supported by PCA of major

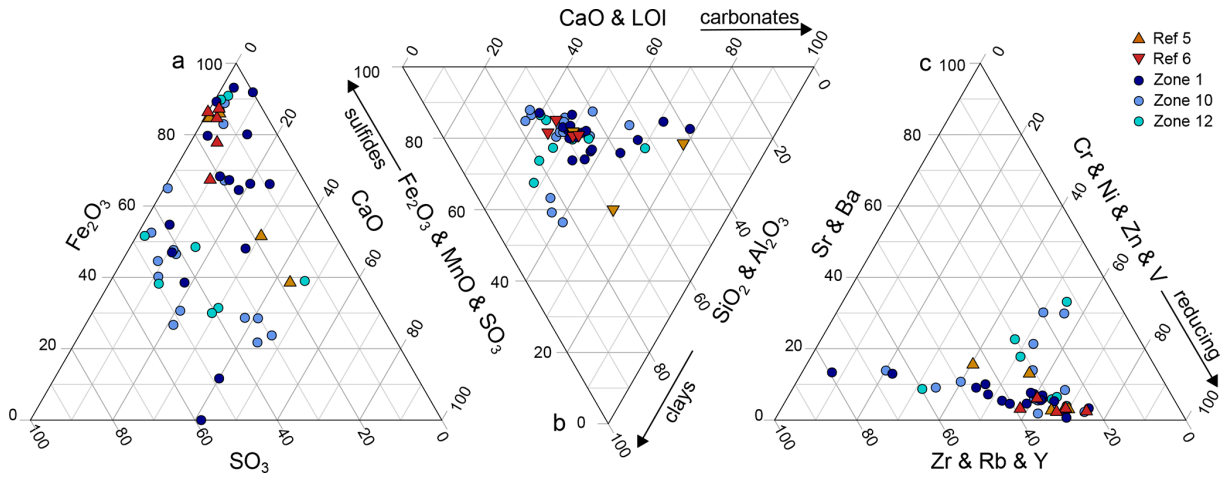

Figure 4. Ternary diagrams showing the relative proportions of selected major and trace elements in solid phase sediments from HC zones and reference zones. **(a)** Major elements: Fe_2O_3–SO_3–CaO, **(b)** major elements grouped by associated mineral fractions: CaO and LOI (carbonate), Fe_2O_3 and MnO and SO_3 (sulfide), and SiO_2 and Al_2O_3 (clay), and **(c)** trace elements grouped by geochemical behavior: Cr, Ni, Zn and V (redox-sensitive), Sr and Ba (calcite-, barite-associated), and Zr, Rb and Y (conservative). Each symbol represents an individual sample. HC zones (blue colors) and reference zones (red colors) largely overlap, the scatter in the HC zones is noticeably larger, indicating a greater variance.

and trace elements (Supplement Figs. S6–S7), where samples from HC zones show greater dispersion along the first principal component (60.7 % and 59.8 % variance explained, respectively), indicating higher variability in both major and trace element composition.

3.4 Organic compound classes across sampling zones

The number of mass spectrometry signals and their distribution across different compound classes (e.g. pure HCs, HCs with O, N, and S atoms), measured in both ionization modes (APPI+ and ESI−) and analyzed in various data representations, appear very similar for both seepage and reference sites. Atomic H/C and O/C ratios derived from assigned molecular formulas showed no significant differences between seep and reference sites. Additionally, the degree of unsaturation (i.e. double bond equivalent, DBE) relative to the number of carbon atoms does not show significant variations in the relative abundance of different compound classes or noticeable differences across sampling sites (Fig. 5, Supplement Fig. 8).

Specific molecular signatures indicative of microbial biomass (e.g. hopanoids) and degraded OM (e.g. humic acids) are also comparable across sampling zones (Fig. 5). Similar to total cell counts, molecular clusters assigned to hopanoid-derived compounds (typically around 6–8 DBE and ∼ 30 carbons) occur in similar abundance at all sites, suggesting comparable microbial population sizes. Likewise, signals corresponding to fatty acids (low DBE, low number of carbons), which can be interpreted as cell remnants or necromass, are evenly distributed. Finally, aromatic compounds which are typically associated with humic substances from highly degraded and refractory OM, are equally present in sediments from all sampling zones. Signatures of seepage-related hydrocarbons, including saturated alkanes and polyaromatic hydrocarbons typically associated with migrated oil and gas, were not detected.

4 Discussion

In the SW Barents Sea, sediments are particularly organic-lean, with TOC values below 0.5 % (Knies and Martinez, 2009). This low organic content enables the detection of discrete HC seeps, as even a slight supply of electron donors can result in a direct increase in the metabolic activity of HC-degrading microbial populations (Joye, 2020). This increase in metabolic activity, along with the resulting geochemical redox changes, can be distinguished from the background signal corresponding to pristine conditions at the seabed. In comparison, any microbial or geochemical signal arising from inconspicuous HC seepage in organic-rich environments would be obscured by ongoing OM breakdown, hampering discrimination of specific microbial populations or metabolic pathways involved in the degradation of discrete HCs.

4.1 Organic signatures of potentially active seepage remain elusive

At seepage sites, we expected a greater diversity and higher concentrations of oxygen-containing compounds in the FT-ICR-MS mass spectra due to the formation of aromatic-ring radicals and by-products (e.g. alcohols, organic acids) during microbial HC degradation (Radovic and Silva, 2025). In sed-

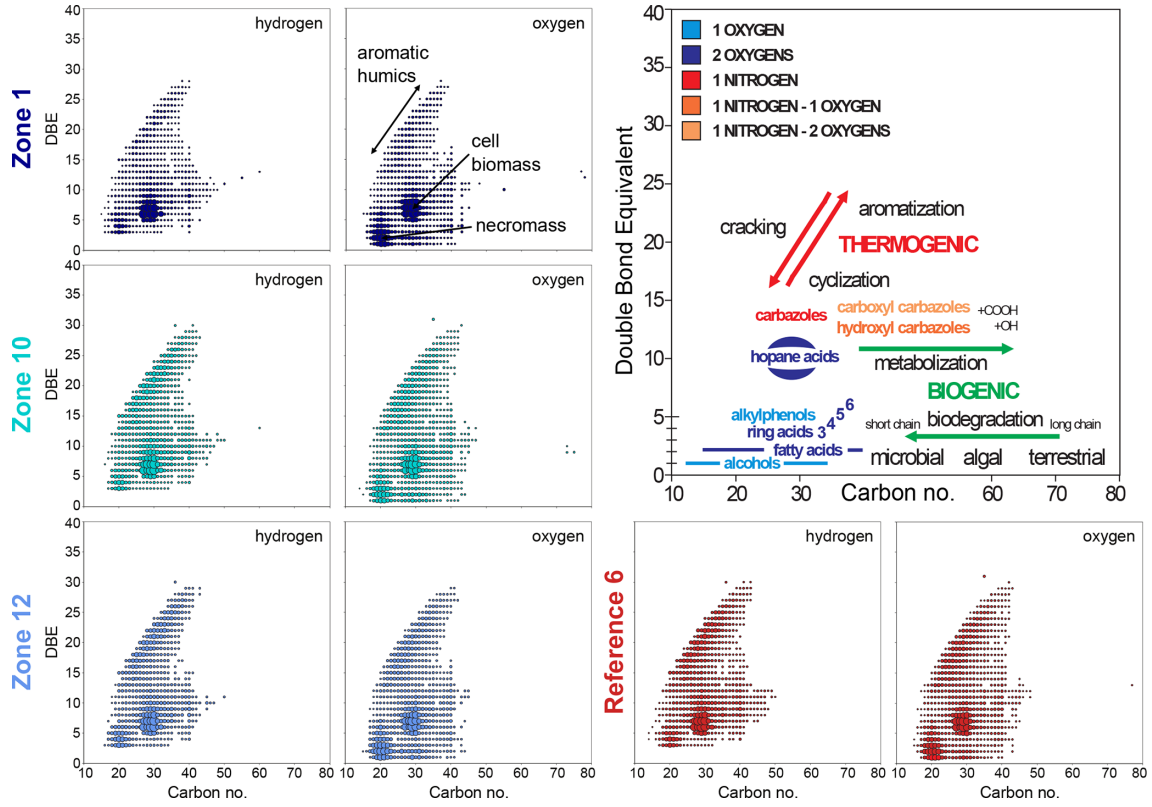

Figure 5. Diagrams for molecular polar compounds identified by FT-ICR-MS in APPI+ mode in sediment extracts from the three hydrocarbon HC zones and one reference zone. (From left to right) Double bond equivalents (DBE) plotted against carbon number for compounds containing hydrogen and oxygen, and simplified interpretative framework of some molecular classes (e.g. aromatic acids, hopane acids, alkylphenols) and the expected shifts related to biogenic (e.g. microbial degradation) vs. thermogenic (e.g. cracking, aromatization) processes.

iments not exposed to seepage, these compounds should be less abundant, with overall a lower proportion of oxygenated components. However, because seepage and reference sites showed similar compound class distributions (Fig. 5; Supplement Fig. S8), our data suggest that HCs had already been degraded at sediment depths below the reach of our cores, or converted into compounds with chain lengths that are too short for FT-ICR-MS detection. Instead, the FT-ICR-MS analysis only captured the background signal of the subseafloor sediments (i.e. biomass, necromass, organic residues), the corresponding compound class concentrations being consistent with similar microbial cell counts across seepage and reference sites (Supplement Fig. 2). Thus, the suitability of this classical oil (and gas) analytical tool (Marshall and Rodgers, 2004) appears to be limited in the context of inconspicuous seepage, indirectly supporting our basic assumption of inconspicuous HC seepage in the HC-affected zones, without any indication for increased microbial biomass at seep sites.

4.2 Hydrocarbon seepage shapes redox zonation with precipitation of carbonate and sulfide minerals

Marine sediments exhibit a clear redox zonation, ranging from the aerobic respiration zone near the surface, transiting through the nitrate, Mn^{4+} and Fe^{3+} reduction zones to the sulfate reduction zone and methanogenesis (Froelich et al., 1979; Jørgensen and Kasten, 2006). In the sulfate reduction zone, sulfate acts as the electron acceptor leading to the production of hydrogen sulfide, bicarbonate, and water. The increase of these compounds in the pore water promotes precipitation of carbonates (e.g. calcite) and sulfide minerals (e.g. pyrite) (Smrzka et al., 2020; Smrzka et al., 2024; Lin et al., 2016; Peckmann et al., 2001). Consequently, the incorporation of calcium, magnesium, strontium, iron, manganese, and trace elements (e.g., Cu, Ni, Zn) into these minerals leads to their depletion in pore water and enrichment in the sediment's inorganic fraction (Smrzka et al., 2019; Schippers and Jørgensen, 2001).

Both sediment geochemistry (Fig. 4, Supplement Figs. S6–S7) and pore water analyses (Fig. 2, Supplement Figs. S3–S5) confirmed the presence of diagenetic carbonates in sediments from HC zones. On the one hand, CaO,

MgO, and Sr abundances increased in the solid phase. On the other hand, pore water Ca^{2+} concentrations decreased while alkalinity simultaneously increased with depth (Fig. 2). In contrast, Mg^{2+} and Sr^{2+} concentrations in pore water remained largely unchanged. Notably, incorporation of Mg^{2+} and Sr^{2+} into carbonate minerals is kinetically restricted compared to Ca^{2+} (Knight et al., 2023; Alkhatib et al., 2022) and, as carbonate precipitation could occur over relatively short time periods (i.e. during active seepage), substitution by pore water Mg^{2+} and Sr^{2+} appeared incomplete, thus their concentrations remained almost unchanged. Although methane-derived carbonates are typically high-Mg calcites or aragonite, we infer that the diagenetic carbonates in our study are likely low-Mg calcites. Alternatively, the recrystallization of metastable carbonate phases (e.g. aragonite) would release Sr^{2+} into the pore water (Hoareau et al., 2010). In contrast to the HC zones, pore water alkalinity, Ca^{2+} and Sr^{2+} concentrations increase with depth at the reference sites, while CaO and Sr contents remain low in the solid phase (Fig. 2, Supplement Fig. S3). These trends indicate that precipitation and dissolution of carbonate minerals occurred (Schneider et al., 2006; Bach, 2024; Hoareau et al., 2010; Smrzka et al., 2019) under seepage and non-seepage conditions, respectively.

Although barium (Ba^{2+}) can theoretically substitute for Ca^{2+} in carbonate minerals, its larger ionic radius and strong affinity for sulfate typically limit its incorporation. Instead, Ba^{2+} precipitates as barite ($BaSO_4$), which tends to dissolve under sulfate-reducing conditions (Carter et al., 2020; von Breymann et al., 1992). Indeed, Ba^{2+} was detectable in pore water in only a few cores from HC-affected Zone 1 (Supplement Fig. S4), where concentrations increased with depth. This pattern suggests localized barite dissolution, likely triggered by reducing conditions and upward fluid flow. Consistently, solid-phase data show elevated Ba^{2+} concentrations in HC-affected zones relative to reference sites (Fig. 4, Supplement Tables S2), indicating barite accumulation through biogeochemical processes linked to HC seepage. These observations highlight the dynamic interplay between sulfate availability, redox zonation, and mineral precipitation at seepage sites, promoting barite dissolution but also sulfide mineralization.

At seepage sites, linear profiles in pore water sulfide revealed upward diffusion (Supplement Fig. S3) and, given the low sulfate reduction rates previously measured in the corresponding interval (Schnabel et al., 2025a), this sulfide likely originates from deeper sediment layers. When reactive metals, such as Fe^{2+}, Mn^{2+}, and other trace metals dissolved in pore water, meet with ascending sulfide, precipitation of metal sulfides occurs, contributing to an accumulation of redox sensitive metals and sulfur in the solid phase. This is in line with observations from e.g. seeps sites in Guaymas basin (Kars et al., 2025). At reference sites, dissolved sulfide is absent while Fe^{2+} and Mn^{2+} concentrations increase in the pore water (Fig. 6, Supplement Fig. S3, Supplement Fig. S4), suggesting that anaerobic respiration of solid-phase Fe(III) and Mn(IV) oxides prevails over sulfate reduction and that precipitation of metal sulfides does not take place, at least not on a quantitatively significant level. Because higher pore water sulfide concentrations in our samples generally correlate with elevated sulfur (i.e. SO_3) (Fig. 6) concentrations in the solid phase, sulfide precipitation and sulfur accumulation allow to distinguish seepage sites from reference sites, where they remain systematically low. This further demonstrates that local differences in sulfide production or flux rates, as well as metal availability, may result from seepage in the sediment.

Besides major element dynamics, HC seepage also alters biogeochemical cycling of trace metals through its influence on redox zonation and authigenic mineral formation, thereby exerting control on their mobility or retention in the sediment column. Trace element incorporation into sulfide minerals vary between oil- and methane-dominated seep environments, with higher concentrations of elements like Mn, Mo, Cu, and Zn often observed in oil seep pyrites (Smrzka et al., 2024). At both seepage and reference zones, redox-sensitive trace metals (e.g. Zn, Ni, and V; Cr to a lesser extent) can be transported in solution upward from deeper sediment layers and precipitate locally depending on sulfate reduction and other redox-dependent activities. At seepage sites, methanotrophic sulfate reduction and AOM-driven processes enhance neoformation of sulfides and carbonates which act as sinks for trace metals at seep sites, in particular pyrite (Smrzka et al., 2019; Smrzka et al., 2024; Miao et al., 2022). In contrast, lower SR activity and lesser mineral precipitation at reference sites allow trace elements to continuously diffuse upward and be captured under suboxic conditions via adsorption or precipitation as iron (oxyhydr)oxides. Altogether, despite similar concentrations in the pore fluid across sampling sites (Supplement Table S2), the degree and depth of occurrence of sulfate reduction govern whether dissolved metal ions are sequestered in specific geochemical zones or bypass the redox gradient. Nevertheless, trace metal concentrations may also vary with redox gradients, precipitation kinetics, and phase-specific affinities (Smrzka et al., 2019), hampering the use of pore water or solid phase concentration as a proxy for HC seepage. Hence, a combined assessment of pore water geochemistry, redox zonation, and authigenic minerals offers a more suitable approach for seepage characterization. Although our bulk sediment geochemical data do not specifically target sulfide mineral phases, these findings highlight the potential of geochemical signatures to record different seepage types.

4.3 Pore water fluxes and diagenetic minerals reflect the dynamics of transient seepage

Linear profiles for pore water alkalinity, SO_4^{2-}, and Ca^{2+} suggest no net turnover within the sampled sediment interval (Schulz, 2006). This stands in contradiction with our obser-

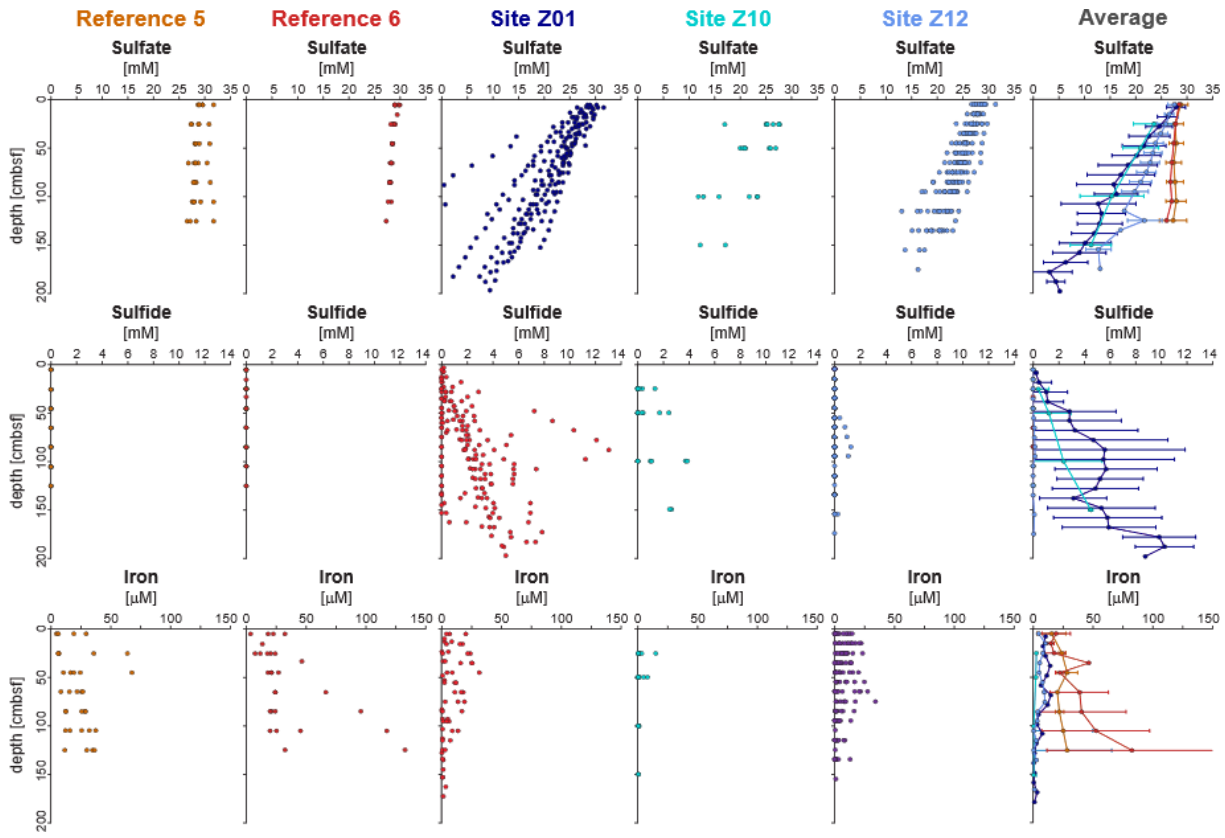

Figure 6. Porewater profiles of sulfate, sulfide, and dissolved iron across five sites, including site averages. In seep-affected cores, iron concentrations decrease where sulfide increases, indicating removal of reactive iron through sulfide precipitation. Sulfate generally decreases with depth across all sites. Error bars represent site-specific averages where applicable.

vations of the solid-phase geochemistry, which is indicative of carbonate and sulfide mineral formation in HC-affected zones. We suggest that the sulfate-methane transition zone (SMTZ), where most sulfide and carbonate precipitation occur, may have undergone temporal and spatial depth fluctuations, driven by variations in HC flux over time. Such fluctuations are well-documented and influenced by multiple factors, including sedimentation rate, temperature, OM availability (Dale et al., 2008) and hydrostatic pressure, which in the Barents Sea is particularly shaped by glacial-interglacial dynamics (Argentino et al., 2021; Nickel et al., 2013).

In the Barents Sea, low sedimentation rates combined with extensive glacial history are inferred to have shaped SMTZ dynamics. During the Last Glacial Maximum (~ 20 ka), grounded ice sheets prevented seawater sulfate diffusion into the sediment in the Barents Sea (Andreassen et al., 2008; Siegert et al., 2001), shifting the SMTZ upward. Following deglaciation (~ 14 ka) (Elverhøi et al., 1993), seawater reoccupied the seafloor, restoring sulfate supply and initiating a progressive downward migration of the SMTZ. Processes such as gas hydrate dissociation and associated methane release during ice retreat (Nickel et al., 2013) further enhanced these dynamics. Comparable patterns have been observed elsewhere in the Barents Sea, where post-glacial rebound and HC flux variations have caused significant SMTZ fluctuations (Argentino et al., 2021).

The occurrence of diagenetic carbonates and sulfides resulting most probably from past AOM processes at the (paleo)SMTZ are therefore best understood as products of these historical boundary conditions. Their accumulation in the sediment, in combination with present-day linear pore water profiles, suggests that the system currently reflects a stage of subdued seepage activity, and consequently deeper SMTZ. Thus, the present-day mineral assemblage provides a cumulative archive of past seepage episodes rather than a snapshot of ongoing processes, highlighting a key limitation of interpreting solid-phase geochemistry alone. Although an increased presence of carbonates and sulfides may be indicative of past redox conditions and fluid flow, these minerals cannot reliably distinguish active from relict seepage. Integration with pore water profiles and other dynamic indicators remains essential to reconstruct seepage history and assess present-day activity.

Overall, our findings align with typical mineralogical signatures of weak HC seeps, commonly with carbonate (CaO) contents of 1 wt %–3 wt % (Rovere et al., 2020; Karaca et al.,

2010) and sulfur (SO_3) concentrations below 1 wt % (Fischer et al., 2012), thereby matching our seepage site values (i.e. 2.1 wt % CaO, 0.8 wt % SO_3). The reference sites of our study exhibit values (i.e. 1.5 wt % CaO, 0.2 wt % SO_3) that are consistent with background diagenesis typically observed in non-seep environments (1–2 wt % CaO, <0.2 wt % SO_3) (Fischer et al., 2012; Karaca et al., 2010). Thus, we observe that carbonate and sulfide enrichments documented in Barents Sea sediments represent the imprint of past seepage episodes, whereas present-day pore water profiles reflect a current state of low, or absent, HC flux within the sampled interval.

4.4 Fine-scale heterogeneity characterizes weak hydrocarbon seepage

The HC zones are affected by inconspicuous, diffuse seepage with very low sulfate flux rates below 1 mmol m^{-2} d^{-1} (Fig. 3). Typical fluxes at seeps range from 1–10 mol m^{-2} d^{-1} for high flux seeps, e.g. Coal Oil Point Seep Field, Santa Barbara, California (Padilla et al., 2019), and 0.1–1 mol m^{-2} d^{-1} for moderate flux seeps, e.g. Northwestern Black Sea (Hu et al., 2012). Since seepage-induced biogeochemical processes, like AOM and concomitant carbonate precipitation, predominantly occur below our sampling depth range (Schnabel et al., 2025a), their effects can be detected only indirectly. For instance, the steeper sulfate gradients observed in the HC zones compared to the reference zones (Fig. 3, Supplement Fig. S3) suggest increased sulfate reduction rates due to HC supply from below. Geochemical fluxes at the seepage sites show considerable variability across individual cores (Fig. 3), which is considered a typical feature of seep environments inherent to localized differences in fluid flow, microbial activity, or redox conditions (Pop Ristova et al., 2015; Foster et al., 2015; Schnabel et al., 2025a). In contrast, reference sites present rather uniform conditions, as they primarily reflect sedimentation, OM input and diffusion at the sediment-water interface rather than seepage.

In addition to variable fluxes reported for cores from seepage sites, the pattern of interconnected geochemical parameters also differs on a spatial scale (Supplement Table S4). While a single pore water species may correlate in all 50 individual cores (e.g. sulfate concentrations and alkalinity), ratios between parameters appear to be different for each core across different HC-affected sites, and even within each individual seepage site sampled. This suggests that, even though similar microbial processes (e.g. denitrification, iron reduction, sulfate reduction), can be expected to take place throughout the sampled area, their degree of intensity and interactions vary on a small spatial scale, leading to considerable local differences both within and between HC zones. In contrast, such correlations are much better both within and across cores from reference sites (Fig. 5), indicating more homogeneous and predictable diagenetic conditions.

5 Conclusions

This study elucidates the geochemical and mineralogical imprints of inconspicuous HC seepage on near-seafloor sediments in the southwestern Barents Sea. Extremely low element fluxes with often complete degradation of HCs in sediment layers below the sampling depth of this study posed significant challenges in the detection of active seepage. This explains why the FT-ICR-MS-based approach was unsuccessful in identifying diagnostic organic compounds, as volatile and short-chained organic compounds cannot be resolved. In contrast, inorganic geochemical signatures provided indirect evidence of seepage-related reductive diagenetic processes. Elevated pore water alkalinity alongside decreasing Ca^{2+} concentrations with depth, substantiated by elemental enrichments in the solid phase were clear indications of carbonate precipitation. In addition, pore water depletion of sulfate and manganese concomitant with increased solid phase sulfide concentrations point towards formation of sulfide minerals. In summary, many geochemical processes along strong seeps can also be directly or indirectly detected for minor HC seeps where the HCs are metabolized below the sampling interval.

Pronounced spatial variability in geochemical gradients across seepage-affected sites was observed, revealing local heterogeneity in fluid flow and redox conditions as a result of variable seepage intensity. Otherwise, correlated geochemical parameters within single cores pointed to consistent coupling with past and present biogeochemical processes. Altogether, these spatial patterns underline the relevance of a targeted sampling strategy to resolve geochemical heterogeneities in the shallow subseafloor, which proves essential for capturing the transient nature of seepage. Fine-scale geochemical variations are easily overlooked but are nonetheless crucial for understanding seep dynamics and differentiating between active and past seepage processes, requiring adequate spatial and temporal coverage and geostatistical techniques.

Data availability. The geochemical data is available on PANGAEA as dataset #974341 and #974346 under digital object identifier https://doi.org/10.1594/PANGAEA.974341 and https://doi.org/10.1594/PANGAEA.974346 (Schnabel et al., 2025b, c).

Supplement. The supplement related to this article is available online at https://doi.org/10.5194/bg-23-1383-2026-supplement.

Team list. The principal investigators of the PROSPECTOMICS project are Jens Kallmeyer (GFZ Helmholtz Centre for Geosciences, Section Geomicrobiology, Telegrafenberg, 14473 Potsdam, Germany), Paul Wilmes (Luxembourg Centre for Systems Biomedicine, University of Luxembourg, Esch-sur-Alzette, Lux-

embourg), Alexander J. Probst (Environmental Metagenomics, Research Center One Health Ruhr of the University Alliance Ruhr, Faculty of Chemistry, University of Duisburg-Essen, Essen, Germany), Dörte Becher (Department of Microbial Proteomics, University of Greifswald, Greifswald, Germany), Thomas Rattei (Computational Systems Biology, Centre for Microbiology and Environmental Systems Science, University of Vienna, Vienna, Austria), and Rolando di Primio (Aker BP ASA, Sandvika, Viken, Norway). The project managers are Aurèle Vuillemin (GFZ Helmholtz Centre for Geosciences, Section Geomicrobiology, Telegrafenberg, 14473 Potsdam, Germany), Cédric L. Laczny (Luxembourg Centre for Systems Biomedicine, University of Luxembourg, Esch-sur-Alzette, Luxembourg), André R. Soares (Environmental Metagenomics, Research Center One Health Ruhr of the University Alliance Ruhr, Faculty of Chemistry, University of Duisburg-Essen, Essen, Germany), and Anke Trautwein-Schult (Department of Microbial Proteomics, University of Greifswald, Greifswald, Germany). Scientists and technicians include Ellen Schnabel (GFZ Helmholtz Centre for Geosciences, Section Geomicrobiology, Telegrafenberg, 14473 Potsdam, Germany), Kai Mangelsdorf (GFZ Helmholtz Centre for Geosciences, Section, Section Organic Geochemistry, Telegrafenberg, 14473 Potsdam, Germany), Steffen Okolski (GFZ Helmholtz Centre for Geosciences, Section Geomicrobiology, Telegrafenberg, 14473 Potsdam, Germany), J. Axel Kitte (GFZ Helmholtz Centre for Geosciences, Section Geomicrobiology, Telegrafenberg, 14473 Potsdam, Germany), Benoit Kunath (Luxembourg Centre for Systems Biomedicine, University of Luxembourg, Esch-sur-Alzette, Luxembourg), Zainab Zafar (Luxembourg Centre for Systems Biomedicine, University of Luxembourg, Esch-sur-Alzette, Luxembourg), Sarah Esser (Environmental Metagenomics, Research Center One Health Ruhr of the University Alliance Ruhr, Faculty of Chemistry, University of Duisburg-Essen, Essen, Germany), Anne Ostrzinski (Department of Microbial Proteomics, University of Greifswald, Greifswald, Germany), Sebastian Grund (Department of Microbial Proteomics, University of Greifswald, Greifswald, Germany), and Alexander Pfundner (Computational Systems Biology, Centre for Microbiology and Environmental Systems Science, University of Vienna, Vienna, Austria).

Author contributions. JK and RdP organized the sampling cruise. ES and JK designed the study and collected samples. ES performed cell counts and analyzed pore water geochemistry under the supervision of JK. XRF measurements were performed under the supervision of JS. FT-ICR-MS analyses of organic extracts were carried out by KM and SP. ES analyzed the data in collaboration with AV, JK and SP. ES wrote the manuscript with input and revisions from all co-authors.

Competing interests. The authors declare that they have no conflict of interest.

Disclaimer. Publisher's note: Copernicus Publications remains neutral with regard to jurisdictional claims made in the text, published maps, institutional affiliations, or any other geographical representation in this paper. The authors bear the ultimate responsibility for providing appropriate place names. Views expressed in the text are those of the authors and do not necessarily reflect the views of the publisher.

Acknowledgements. We thank all crew members of the RV *Sverdrup II*, Steffen Okolski, J. Axel Kitte and Edgar Kutschera for their great help during the sampling cruise. The help of Steffen Okolski in pore water analyses is acknowledged. We acknowledge the support of Anja Schleicher, Andrea Gottsche and Heike Rothe in performing the XRF and ICP-MS measurements, including sample melting and instrument operation. Sabine Kasten and Bo Liu are thanked for advices on data processing.

Financial support. This research has received funding from the European Union's Horizon 2020 research and innovation programme under grant agreement no. 899667.

The article processing charges for this open-access publication were covered by the GFZ Helmholtz Centre for Geosciences.

Review statement. This paper was edited by Mark Lever and reviewed by Hongchen Jiang and one anonymous referee.

References

Abrams, M. A.: Significance of hydrocarbon seepage relative to petroleum generation and entrapment, Marine and Petroleum Geology, 22, 457–477, https://doi.org/10.1016/j.marpetgeo.2004.08.003, 2005.

Abrams, M. A.: Marine seepage variability and its impact on evaluating the surface migrated hydrocarbon seep signal, Marine and Petroleum Geology, 121, 13, https://doi.org/10.1016/j.marpetgeo.2020.104600, 2020.

Alkhatib, M., Qutob, M., Alkhatib, S., and Eisenhauer, A.: Influence of precipitation rate and temperature on the partitioning of magnesium and strontium in calcite overgrowths, Chemical Geology, 599, https://doi.org/10.1016/j.chemgeo.2022.120841, 2022.

Andreassen, K., Laberg, J. S., and Vorren, T. O.: Seafloor geomorphology of the SW Barents Sea and its glacidynamic implications, Geomorphology, 97, 157–177, https://doi.org/10.1016/j.geomorph.2007.02.050, 2008.

Argentino, C., Waghorn, K. A., Vadakkepuliyambatta, S., Polteau, S., Bunz, S., and Panieri, G.: Dynamic and history of methane seepage in the SW Barents Sea: new insights from Leirdjupet Fault Complex, Sci. Rep., 11, 4373, https://doi.org/10.1038/s41598-021-83542-0, 2021.

Bach, L. T.: The additionality problem of ocean alkalinity enhancement, Biogeosciences, 21, 261–277, https://doi.org/10.5194/bg-21-261-2024, 2024.

Berner, R. A.: A new geochemical classification of sedimentary environments, Journal of Sedimentary Research, 51, 359–365, https://doi.org/10.1306/212f7c7f-2b24-11d7-8648000102c1865d, 1981.

Bowles, M. W., Mogollon, J. M., Kasten, S., Zabel, M., and Hinrichs, K. U.: Global rates of marine sulfate reduction and impli-

cations for sub-sea-floor metabolic activities, Science, 344, 889–891, https://doi.org/10.1126/science.1249213, 2014.

Bradley, J. A., Arndt, S., Amend, J. P., Burwicz, E., Dale, A. W., Egger, M., and LaRowe, D. E.: Widespread energy limitation to life in global subseafloor sediments, Sci. Adv., 6, eaba0697, https://doi.org/10.1126/sciadv.aba0697, 2020.

Brown, M. B. and Forsythe, A. B.: Robust Tests for the Equality of Variances, Journal of the American Statistical Association, 69, 364–367, https://doi.org/10.1080/01621459.1974.10482955, 1974.

Carter, S. C., Paytan, A., and Griffith, E. M.: Toward an Improved Understanding of the Marine Barium Cycle and the Application of Marine Barite as a Paleoproductivity Proxy, Minerals, 10, https://doi.org/10.3390/min10050421, 2020.

Chavez, F. P., Messié, M., and Pennington, J. T.: Marine primary production in relation to climate variability and change, Annual Review of Marine Science, 3, 227–260, https://doi.org/10.1146/annurev.marine.010908.163917, 2011.

Ciotoli, G., Procesi, M., Etiope, G., Fracassi, U., and Ventura, G.: Influence of tectonics on global scale distribution of geological methane emissions, Nat. Commun., 11, 2305, https://doi.org/10.1038/s41467-020-16229-1, 2020.

Cline, J. D.: Spectrophotometric Determination of Hydrogen Sulfide in Natural Waters1, Limnol. Oceanogr., 14, 454–458, https://doi.org/10.4319/lo.1969.14.3.0454, 1969.

Dale, A. W., Aguilera, D. R., Regnier, P., Fossing, H., Knab, N. J., and Jorgensen, B. B.: Seasonal dynamics of the depth and rate of anaerobic oxidation of methane in Aarhus Bay (Denmark) sediments, Journal of Marine Research, 66, 127–155, https://elischolar.library.yale.edu/journal_of_marine_research/190/ (last access: 19 February 2026), 2008.

de Groot, T. R., Kalenitchenko, D., Moser, M., Argentino, C., Panieri, G., Lindgren, M., Dølven, K. O., Ferré, B., Svenning, M. M., and Niemann, H.: Methanotroph activity and connectivity between two seep systems north off Svalbard, Frontiers in Earth Science, 12, https://doi.org/10.3389/feart.2024.1287226, 2024.

Dong, H., Jaisi, D. P., Kim, J., and Zhang, G.: Microbe-clay mineral interactions, American Mineralogist, 94, 1505–1519, https://doi.org/10.2138/am.2009.3246, 2009.

Doré, A. G.: Barents Sea Geology, Petroleum Resources and Commercial Potencial, ARCTIC, 48, 207–221, 1995.

Edenborn, H. M., Paquin, Y., and Chateauneuf, G.: Bacterial contribution to manganese oxidation in a deep coastal sediment, Estuarine, Coastal and Shelf Science, 21, 801–815, https://doi.org/10.1016/0272-7714(85)90074-5, 1985.

Eichhubl, P., Davatzes, N. C., and Becker, S. P.: Structural and diagenetic control of fluid migration and cementation along the Moab fault, Utah, Aapg Bulletin, 93, 653–681, https://doi.org/10.1306/02180908080, 2009.

Elverhøi, A. and Solheim, A.: The Barents Sea ice sheet – a sedimentological discussion, Polar Research, 1, 23–42, https://doi.org/10.3402/polar.v1i1.6968, 1983.

Elverhøi, A., Fjeldskaar, W., Solheim, A., Nyland-Berg, M., and Russwurm, L.: The Barents Sea Ice Sheet – a model of its growth and decay during the last ice maximum, Quaternary Science Reviews, 12, 11, https://doi.org/10.1016/0277-3791(93)90025-H, 1993.

Etiope, G.: Natural Gas Seepage – The Earth's Hydrocarbon Degassing, Springer, ISBN 978-3-319-14601-0, 2015.

Faleide, J. I., Gudlaugsson, S. T., and Jacquart, G.: Evolution of the western Barents Sea, Marine and Petroleum Geology, 1, 123–150, https://doi.org/10.1016/0264-8172(84)90082-5, 1984.

Fischer, D., Sahling, H., Nöthen, K., Bohrmann, G., Zabel, M., and Kasten, S.: Interaction between hydrocarbon seepage, chemosynthetic communities, and bottom water redox at cold seeps of the Makran accretionary prism: insights from habitat-specific pore water sampling and modeling, Biogeosciences, 9, 2013–2031, https://doi.org/10.5194/bg-9-2013-2012, 2012.

Foster, K. L., Stern, G. A., Carrie, J., Bailey, J. N., Outridge, P. M., Sanei, H., and Macdonald, R. W.: Spatial, temporal, and source variations of hydrocarbons in marine sediments from Baffin Bay, Eastern Canadian Arctic, Sci. Total Environ., 506/507, 430–443, https://doi.org/10.1016/j.scitotenv.2014.11.002, 2015.

Froelich, P. N., Klinkhammer, G. P., Bender, M. L., Luedtke, N. A., Heath, G. R., Cullen, D., Dauphin, P., Hammond, D., Hartman, B., and Maynard, V.: Early oxidation of organic matter in pelagic sediments of the eastern equatorial Atlantic: suboxic diagenesis, Geochemica et Cosmochimica Acta, 43, 1975–1090, https://doi.org/10.1016/0016-7037(79)90095-4, 1979.

Gabrielsen, R. H., Faerseth, R. B., Jensen, L. N., Kalheim, J. E., and Riis, F.: Structual elements of the Norwegian continental shelf, Part 1: The Barents Sea Region, NPD Bulletin, 6, 1–33, 1990.

Heggland, R.: Gas seepage as an indicator of deeper prospective reservoirs. A study based on exploration 3D seismic data, Marine and Petroleum Geology, 15, 1–9, https://doi.org/10.1016/S0264-8172(97)00060-3, 1998.

Hinrichs, K. U., Hayes, J. M., Sylva, S. P., Brewer, P. G., and DeLong, E. F.: Methane-consuming archaebacteria in marine sediments, Nature, 398, 802–805, https://doi.org/10.1038/19751, 1999.

Hoareau, G., Monnin, C., and Odonne, F.: A study of celestine equilibrium in marine sediments using the entire ODP/IODP porewater data base, Geochimica et Cosmochimica Acta, 74, 3925–3937, https://doi.org/10.1016/j.gca.2010.03.033, 2010.

Hu, L., Yvon-Lewis, S. A., Kessler, J. D., and MacDonald, I. R.: Methane fluxes to the atmosphere from deepwater hydrocarbon seeps in the northern Gulf of Mexico, Journal of Geophysical Research: Oceans, 117, https://doi.org/10.1029/2011jc007208, 2012.

Hu, T., Luo, M., Qi, Y., He, D., Chen, L., Xu, Y., and Chen, D.: Molecular evidence for the production of labile, sulfur-bearing dissolved organic matter in the seep sediments of the South China Sea, Water Res., 233, 119732, https://doi.org/10.1016/j.watres.2023.119732, 2023.

Huerta-Diaz, M. A. and Morse, J. W.: Pyritization of trace metals in anoxic marine sediments, Geochimica et Cosmochimica Acta, 56, 2681–2702, https://doi.org/10.1016/0016-7037(92)90353-k, 1992.

Hunt, J. M.: Petroleum Geochemistry and Geology, W.H. Freeman & Co Ltd, New York, ISBN 9780716724414, 1995.

Hvoslef, S., Christie, O. H. J., Sassen, R., Kennicutt, M. C., Requejo, A. G., and Brooks, J. M.: Test of a new surface geochemistry tool for resource prediction in frontier areas, Marine and Petroleum Geology, 13, 107–124, https://doi.org/10.1016/0264-8172(95)00032-1, 1996.

Iversen, N. and Jørgensen, B. B.: Diffusion coefficents of sulfate and methane in marine sediments: Influence of

porosity, Geochemica et Cosmochemica Acta, 57, 571–778, https://doi.org/10.1016/0016-7037(93)90368-7, 1993.

Johansen, S. E., Ostisty, B. K., Birkeland, ø., Fedorovsky, Y. F., Martirosjan, V. N., Bruun Christensen, O., Cheredeev, S. I., Ignatenko, E. A., and Margulis, L. S.: Hydrocarbon potential in the Barents Sea region: play distribution and potential, Norwegian Petroleum Society Special Publications, 2, 273–320, https://doi.org/10.1016/B978-0-444-88943-0.50024-1, 1993.

Jørgensen, B. B.: Mineralization of organic matter in the sea bed – the role of sulphate reduction, Nature, 296, 643–645, https://doi.org/10.1038/296643a0, 1982.

Jørgensen, B. B. and Kasten, S.: Sulfur Cycling and Methane Oxidation, in: Marine Geochemistry, 271–309, https://doi.org/10.1007/3-540-32144-6_8, 2006.

Jørgensen, B. B., Findlay, A. J., and Pellerin, A.: The Biogeochemical Sulfur Cycle of Marine Sediments, Front Microbiol., 10, 849, https://doi.org/10.3389/fmicb.2019.00849, 2019.

Joye, S. B.: The Geology and Biogeochemistry of Hydrocarbon Seeps, Annual Review of Earth and Planetary Sciences, 48, 205–231, https://doi.org/10.1146/annurev-earth-063016-020052, 2020.

Joye, S. B., Boetius, A., Orcutt, B. N., Montoya, J. P., Schulz, H. N., Erickson, M. J., and Lugo, S. K.: The anaerobic oxidation of methane and sulfate reduction in sediments from Gulf of Mexico cold seeps, Chemical Geology, 205, 219–238, https://doi.org/10.1016/j.chemgeo.2003.12.019, 2004.

Joye, S. B., Bowles, M. W., and Ziervogel, K.: Marine Biogeochemical Cycles, in: The Marine Microbiome, Springer, Cham, 623–671, https://doi.org/10.1007/978-3-030-90383-1_15, 2022.

Judd, A. and Hovland, M.: Seabed fluid flow – The impact on geology, biology and the marine environment, Cambridge University Press, https://doi.org/10.1017/cbo9780511535918, 2009.

Kallmeyer, J., Smith, D. C., Spivack, A. J., and D'Hondt, S.: New cell extraction procedure applied to deep subsurface sediments, Limnology and Oceanography: Methods, 6, 236–245, https://doi.org/10.4319/lom.2008.6.236, 2008.

Karaca, D., Hensen, C., and Wallmann, K.: Controls on authigenic carbonate precipitation at cold seeps along the convergent margin off Costa Rica, Geochemistry, Geophysics, Geosystems, 11, https://doi.org/10.1029/2010gc003062, 2010.

Kars, M. A. C., Pastor, L., Burin, C., and Koornneef, L. M. T.: Data report: characterization of iron oxides and iron sulfides in sediments from IODP Expedition 385 Sites U1549 and U1552 using rock magnetism and geochemistry, in: Proceedings of the International Ocean Discovery Program, edited by: Teske, A., Lizarralde, D., Höfig, T. W., and the Expedition 385 Scientists, Volume 385, 19 pp., International Ocean Discovery Program, https://doi.org/10.14379/iodp.proc.385.207.2025, 2025.

Kasten, S. and Jørgensen, B. B.: Sulfate Reduction in Marine Sediments, in: Marine Geochemistry, Springer, Heidelberg, 263–281, https://doi.org/10.1007/978-3-662-04242-7_8, 2000.

Kim, J., Dong, H. L., Seabaugh, J., Newell, S. W., and Eberl, D. D.: Role of microbes in the smectite-to-illite reaction, Science, 303, 830–832, https://doi.org/10.1126/science.1093245, 2004.

Knies, J. and Martinez, P.: Organic matter sedimentation in the western Barents Sea region: Terrestrial and marine contribution based on isotopic composition and organic nitrogen content, Norwegian Journal of Geology, 89, 79–89, 2009.

Knight, A. W., Harvey, J. A., Shohel, M., Lu, P., Cummings, D., and Ilgen, A. G.: The combined effects of Mg^{2+} and Sr^{2+} incorporation during $CaCO_3$ precipitation and crystal growth, Geochimica et Cosmochimica Acta, 345, 16–33, https://doi.org/10.1016/j.gca.2023.01.021, 2023.

Langrock, U., Stein, R., Lipinski, M., and Brumsack, H.-J.: Paleoenvironment and sea-level change in the early Cretaceous Barents Sea – implications from near-shore marine sapropels, GeoMarine Letters, 23, 34–42, https://doi.org/10.1007/s00367-003-0122-5, 2003.

Larssen, G. B., Elvebakk, G., Henriksen, L. B., Kristensen, S.-E., Nilsson, I., Samuelsberg, T. J., Svana, T. A., Stemmerik, L., and Worsley, D.: Upper Palaeozoic lithostratigraphy of the Southern Norwegian Barents Sea, Norsk Geologisk Undersøkelser, Bull., 444, 43, https://www.researchgate.net/publication/312656540_Upper_Palaeozoic_lithostratigraphy_of_the_southern_part_of_the_Norwegian_Barents_Sea (last access: 9 February 2026), 2002.

Leifer, I., Boles, J. R., Luyendyk, B. P., and Clark, J. F.: Transient discharges from marine hydrocarbon seeps: spatial and temporal variability, Environmental Geology, 46, 1038–1052, https://doi.org/10.1007/s00254-004-1091-3, 2004.

Lin, Z., Sun, X., Peckmann, J., Lu, Y., Xu, L., Strauss, H., Zhou, H., Gong, J., Lu, H., and Teichert, B. M. A.: How sulfate-driven anaerobic oxidation of methane affects the sulfur isotopic composition of pyrite: A SIMS study from the South China Sea, Chemical Geology, 440, 26–41, https://doi.org/10.1016/j.chemgeo.2016.07.007, 2016.

Mann, H. B. and Whitney, D. R.: On a Test of Whether one of Two Random Variables is Stochastically Larger than the Other, The Annals of Mathematical Statistics, 18, 50–60, https://doi.org/10.1214/aoms/1177730491, 1947.

Marín, D., Helleren, S., Escalona, A., Olaussen, S., Cedeño, A., Nøhr-Hansen, H., and Ohm, S.: The Middle Jurassic to lowermost Cretaceous in the SW Barents Sea: Interplay between tectonics, coarse-grained sediment supply and organic matter preservation, Basin Research, 33, 1033–1055, https://doi.org/10.1111/bre.12504, 2020.

Marshall, A. G. and Rodgers, R. P.: Petroleomics: the next grand challenge for chemical analysis, Acc. Chem. Res., 37, 53–59, https://doi.org/10.1021/ar020177t, 2004.

Matheron, G.: Principles of geostatistics, Economic Geology, 58, 1246–1266, https://doi.org/10.2113/gsecongeo.58.8.1246, 1963.

Miao, X., Feng, X., Li, J., Liu, X., Liang, J., Feng, J., Xiao, Q., Dan, X., and Wei, J.: Enrichment mechanism of trace elements in pyrite under methane seepage, Geochemical Perspectives Letters, 21, 18–22, https://doi.org/10.7185/geochemlet.2211, 2022.

Middelburg, J. J.: Reviews and syntheses: to the bottom of carbon processing at the seafloor, Biogeosciences, 15, 413–427, https://doi.org/10.5194/bg-15-413-2018, 2018.

Nickel, J. C., di Primio, R., Mangelsdorf, K., Stoddart, D., and Kallmeyer, J.: Characterization of microbial activity in pockmark fields of the SW-Barents Sea, Marine Geology, 332–334, 152–162, https://doi.org/10.1016/j.margeo.2012.02.002, 2012.

Nickel, J. C., di Primio, R., Kallmeyer, J., Hammer, Ø., Horsfield, B., Stoddart, D., Brunstad, H., and Mangelsdorf, K.: Tracing the origin of thermogenic hydrocarbon signals in pockmarks from the southwestern Barents Sea, Organic Geochemistry, 63, 73–84, https://doi.org/10.1016/j.orggeochem.2013.08.008, 2013.

Orphan, V. J., Hinrichs, K. U., Ussler III, W., Paull, C. K., Taylor, L. T., Sylva, S. P., Hayes, J. M., and Delong, E. F.: Comparative analysis of methane-oxidizing archaea and sulfate-reducing bacteria in anoxic marine sediments, Appl. Environ. Microbiol., 67, 1922–1934, https://doi.org/10.1128/AEM.67.4.1922-1934.2001, 2001.

Padilla, A. M., Loranger, S., Kinnaman, F. S., Valentine, D. L., and Weber, T. C.: Modern Assessment of Natural Hydrocarbon Gas Flux at the Coal Oil Point Seep Field, Santa Barbara, California, Journal of Geophysical Research: Oceans, 124, 2472–2484, https://doi.org/10.1029/2018jc014573, 2019.

Pearson, K.: Note on regression and inheritance in the case of two parents, Proceedings of the Royal Society of London, 58, 240–242, https://doi.org/10.1098/rspl.1895.0041, 1895.

Pebesma, E. J.: Multivariable geostatistics in S: the gstat package, Computers & Geosciences, 30, 683–691, https://doi.org/10.1016/j.cageo.2004.03.012, 2004.

Peckmann, J., Reimer, A., Luth, U., Luth, C., Hansen, B. T., Heinicke, C., Hoefs, J., and Reitner, J.: Methane-derived carbonates and authigenic pyrite from the northwestern Black Sea, Marine Geology, 177, 129–150, https://doi.org/10.1016/S0025-3227(01)00128-1, 2001.

Poetz, S., Horsfield, B., and Wilkes, H.: Maturity-Driven Generation and Transformation of Acidic Compounds in the Organic-Rich Posidonia Shale as Revealed by Electrospray Ionization Fourier Transform Ion Cyclotron Resonance Mass Spectrometry, Energy & Fuels, 28, 4877–4888, https://doi.org/10.1021/ef500688s, 2014.

Pop Ristova, P., Wenzhofer, F., Ramette, A., Felden, J., and Boetius, A.: Spatial scales of bacterial community diversity at cold seeps (Eastern Mediterranean Sea), ISME J., 9, 1306–1318, https://doi.org/10.1038/ismej.2014.217, 2015.

Radovic, J. R. and Silva, R. C.: Ultrahigh-Resolution Mass Spectrometry Advances for Biogeochemical Analysis: From Seafloor Sediments to Petroleum and Marine Oil Spills, J. Am. Soc. Mass. Spectrom., 36, 7–33, https://doi.org/10.1021/jasms.4c00266, 2025.

Rasheed, M. A., Lakshmi, M., Rao, P. L. S., Kalpana, M. S., Dayal, A. M., and Patil, D. J.: Geochemical evidences of trace metal anomalies for finding hydrocarbon microseepage in the petroliferous regions of the Tatipaka and Pasarlapudi areas of Krishna Godavari Basin, India, Petroleum Science, 10, 19–29, https://doi.org/10.1007/s12182-013-0245-x, 2013.

R Core Team: The R Project for Statistical Computing, https://www.R-project.org/ (last access: 12 June 2023), 2022.

Rovere, M., Mercorella, A., Frapiccini, E., Funari, V., Spagnoli, F., Pellegrini, C., Bonetti, A. S., Veneruso, T., Tassetti, A. N., Dell'Orso, M., Mastroianni, M., Giuliani, G., De Marco, R., Fabi, G., Ciccone, F., and Antoncecchi, I.: Geochemical and Geophysical Monitoring of Hydrocarbon Seepage in the Adriatic Sea, Sensors (Basel), 20, https://doi.org/10.3390/s20051504, 2020.

Røy, H., Kallmeyer, J., Adhikari, R. R., Pockalny, R., Jørgensen, B. B., and D'Hondt, S.: Aerobic microbial respiration in 86-million-year-old deep-sea red clay, Science, 336, 922–925, https://doi.org/10.1126/science.1219424, 2012.

Sættem, J., Rise, L., and Westgaard, D. A.: Composition and properties of glacigenic sediments in the southwestern Barents Sea, Marine Geotechnology, 10, 229–255, https://doi.org/10.1080/10641199109379893, 1991.

Schippers, A. and Jørgensen, B. B.: Oxidation of pyrite and iron sulfide by manganese dioxide in marine sediments, Geochimica et Cosmochimica Acta, 65, 915–922, https://doi.org/10.1016/s0016-7037(00)00589-5, 2001.

Schnabel, E., Vuillemin, A., Laczny, C. C., Kunath, B. J., Soares, A. R., Probst, A. J., Di Primio, R., Kallmeyer, J., and the PROSPECTOMICS Consortium: Influence of minor hydrocarbon seepage on sulfur cycling in marine subsurface sediments, Biogeosciences, 22, 767–784, https://doi.org/10.5194/bg-22-767-2025, 2025a.

Schnabel, E., Vuillemin, A., Laczny, C. C., Kunath, B. J., Soares, A. R., Di Primo, R., Kallmeyer, J., and PROSPECTOMICS, Consortium: Pore water solutes, total cell counts, dissolved gases and sulfate reduction rates of the 50 gravity cores of the PROSPECTOMICS project, PANGAEA [data set], https://doi.org/10.1594/PANGAEA.974341, 2025b.

Schnabel, E., Vuillemin, A., Laczny, C. C., Kunath, B. J., Soares, A. R., Di Primo, R., Kallmeyer, J., and PROSPECTOMICS, Consortium: XRF measurements of major oxides and trace elements on bulk sediment of the 50 gravity cores of the PROSPECTOMICS project, PANGAEA [data set], https://doi.org/10.1594/PANGAEA.974346, 2025c.

Schneider, R. R., Schulz, H. D., and Hensen, C.: Marine Carbonates: Their Formation and Destruction, in: Marine Geochemistry, edited by: Schulz, H. D. and Zabel, M., Springer, Berlin, Heidelberg, 311–337, https://doi.org/10.1007/3-540-32144-6_9, 2006.

Schulz, H. D.: Quantification of Early Diagenesis: Dissolved Constituents in Pore Water and Signals in the Solid Phase, in: Marine Geochemistry, 73–124, https://doi.org/10.1007/3-540-32144-6_3, 2006.

Sedgwick, P.: Pearson's correlation coefficient, BMJ, 345, e4483–e4483, https://doi.org/10.1136/bmj.e4483, 2012.

Seeberg-Elverfeldt, J., Schluter, M., Feseker, T., and Kolling, M.: Rhizon sampling of porewaters near the sediment-water interface of aquatic systems, Limnol. Oceanogr.-Meth., 3, 361–371, https://doi.org/10.4319/lom.2005.3.361, 2005.

Sert, M. F., D'Andrilli, J., Gründger, F., Niemann, H., Granskog, M. A., Pavlov, A. K., Ferré, B., and Silyakova, A.: Compositional Differences in Dissolved Organic Matter Between Arctic Cold Seeps Versus Non-Seep Sites at the Svalbard Continental Margin and the Barents Sea, Frontiers in Earth Science, 8, https://doi.org/10.3389/feart.2020.552731, 2020.

Siegert, M. J., Dowdeswell, J. A., Hald, M., and Svendsen, J. I.: Modelling the Eurasian Ice Sheet through a full (Weichselian) glacial cycle, Global and Planetary Change, 31, 367–385, https://doi.org/10.1016/S0921-8181(01)00130-8, 2001.

Smrzka, D., Zwicker, J., Bach, W., Feng, D., Himmler, T., Chen, D., and Peckmann, J.: The behavior of trace elements in seawater, sedimentary pore water, and their incorporation into carbonate minerals: a review, Facies, 65, 47, https://doi.org/10.1007/s10347-019-0581-4, 2019.

Smrzka, D., Feng, D., Himmler, T., Zwicker, J., Hu, Y., Monien, P., Tribovillard, N., Chen, D., and Peckmann, J.: Trace elements in methane-seep carbonates: Potentials, limitations, and perspectives, Earth-Science Reviews, 208, https://doi.org/10.1016/j.earscirev.2020.103263, 2020.

Smrzka, D., Lin, Z., Monien, P., Chen, T., Bach, W., Peckmann, J., and Bohrmann, G.: Pyrite-based trace element fingerprints for methane and oil seepage, Geochemical Perspectives Letters, 29, 33–37, https://doi.org/10.7185/geochemlet.2409, 2024.

Tribovillard, N., du Châtelet, E. A., Gay, A., Barbecot, F., Sansjofre, P., and Potdevin, J.-L.: Geochemistry of cold seepage-impacted sediments: Per-ascensum or per-descensum trace metal enrichment?, Chemical Geology, 340, 1–12, https://doi.org/10.1016/j.chemgeo.2012.12.012, 2013.

Viollier, E., Inglett, P. W., Hunter, K., Roychoudhury, A. N., and Van Cappellen, P.: The ferrozine method revisited: Fe(II)/Fe(III) determination in natural waters, Applied Geochemistry, 15, 785–790, https://doi.org/10.1016/s0883-2927(99)00097-9, 2000.

von Breymann, M. T., Brumsack, H., and Emeis, K. C.: Depositional and Diagenetic Behavior of Barium in the Japan Sea, in: Proceedings of the Ocean Drilling Program, 127/128 Part 1, Scientific Results, https://doi.org/10.2973/odp.proc.sr.127128-1.168.1992, 1992.

Vuillemin, A., Vargas, S., Coskun, O. K., Pockalny, R., Murray, R. W., Smith, D. C., D'Hondt, S., and Orsi, W. D.: Atribacteria Reproducing over Millions of Years in the Atlantic Abyssal Subseafloor, mBio, 11, https://doi.org/10.1128/mBio.01937-20, 2020.

Vuillemin, A., Morlock, M., Paskin, A., Benning, L. G., Henny, C., Kallmeyer, J., Russell, J. M., and Vogel, H.: Authigenic minerals reflect microbial control on pore waters in a ferruginous analogue, Geochemical Perspectives Letters, 28, 20–26, https://doi.org/10.7185/geochemlet.2339, 2023a.

Vuillemin, A., Mayr, C., Schuessler, J. A., Friese, A., Bauer, K. W., Lücke, A., Heuer, V. B., Glombitza, C., Henny, C., von Blanckenburg, F., Russell, J. M., Bijaksana, S., Vogel, H., Crowe, S. A., and Kallmeyer, J.: A one-million-year isotope record from siderites formed in modern ferruginous sediments, GSA Bulletin, 135, 504–522, https://doi.org/10.1130/b36211.1, 2023b.

Wickham, H.: ggplot2, Springer-Verlag, New York, 260 pp., https://doi.org/10.1007/978-3-319-24277-4, 2016.

Widdel, F., Knittel, K., and Galushko, A.: Anaerobic Hydrocarbon-Degrading Microorganisms: An Overview, in: Handbook of Hydrocarbon and Lipid Microbiology, Springer, Berlin, Heidelberg, 1997–2021, https://doi.org/10.1007/978-3-540-77587-4, 2010.

Yergin, D.: The Prize: The Epic Quest for Oil, Money & Power, Free Press, ISBN 9781847376466, 2009.

Zhang, X., Wu, K., Han, Z., Chen, Z., Liu, Z., Sun, Z., Shao, L., Zhao, Z., and Zhou, L.: Microbial diversity and biogeochemical cycling potential in deep-sea sediments associated with seamount, trench, and cold seep ecosystems, Front. Microbiol., 13, 1029564, https://doi.org/10.3389/fmicb.2022.1029564, 2022.

Zhao, R. X., Xue, H. T., Lu, S. F., Greenwell, and Erastova, V.: Revealing crucial effects of reservoir environment and hydrocarbon fractions on fluid behavior in kaolinite pores, Chem. Eng. J., 489, https://doi.org/10.1016/j.cej.2024.151362, 2024.